Article

Interstitial Cell Remodeling Promotes Aberrant Adipogenesis in Dystrophic Muscles

Graphical Abstract

Highlights

- Single-cell RNA-seq reveals an altered cell landscape in dystrophic skeletal muscle

- Classification of interstitial stem cell states from healthy and dystrophic muscle

- Adipo-regulatory cells (Aregs) block adipogenesis through GDF10 secretion

- The amount of Aregs decreases in dystrophic muscle, thereby increasing fat depots

Authors

Jordi Camps, Natacha Breuls, Alejandro Sifrim, ..., Yvan Torrente, Thierry Voet, Maurilio Sampaolesi

Correspondence

maurilio.sampaolesi@kuleuven.be

In Brief

Camps et al. describe a cell population that blocks fat turnover in the skeletal muscle by single-cell analysis. Furthermore, they show that this population acts through GDF10 secretion and is reduced in dystrophic muscle. This could be an essential turning point in the progressive deterioration of muscular dystrophy patients.
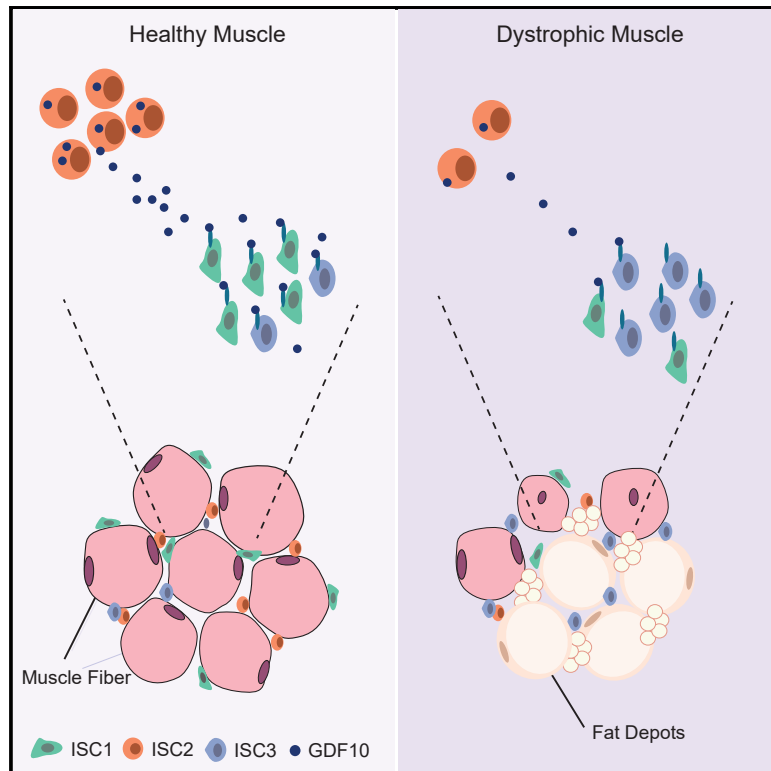
CellPress

Article

Interstitial Cell Remodeling Promotes Aberrant Adipogenesis in Dystrophic Muscles

Jordi Camps,[1,2,10] Natacha Breuls,[1,10] Alejandro Sifrim,[3,4] Nefele Giarratana,[1] Marlies Corvelyn,[1] Laura Danti,[1] Hanne Grosemans,[1] Sebastiaan Vanuytven,[3] Irina Thiry,[5] Marzia Belicchi,[6] Mirella Meregalli,[6] Khrystyna Platko,[7] Melissa E. MacDonald,[7] Richard C. Austin,[7] Rik Gijsbers,[5] Giulio Cossu,[8] Yvan Torrente,[6] Thierry Voet,[3,4] and Maurilio Sampaolesi[1,9,11,*]

[1]Laboratory of Translational Cardiomyology, Department of Development and Regeneration, Stem Cell Research Institute, KU Leuven, 3000 Leuven, Belgium
[2]Bayer AG, Research & Development, Pharmaceuticals, 13353 Berlin, Germany
[3]Laboratory of Reproductive Genomics, Department of Human Genetics, KU Leuven, 3000 Leuven, Belgium
[4]Wellcome Genome Campus, Wellcome Sanger Institute, Cambridge CB10 1SA, UK
[5]Laboratory for Molecular Virology and Gene Therapy, and Leuven Viral Vector Core, KU Leuven, 3000 Leuven, Belgium
[6]Department of Pathophysiology and Transplantation, Università degli Studi di Milano, Fondazione IRCCS Ca' Granda Ospedale Maggiore Policlinico, Centro Dino Ferrari, 20122 Milan, Italy
[7]Department of Medicine, The Research Institute of St. Joe's Hamilton, Hamilton Centre for Kidney Research, McMaster University, Hamilton, ON L8N 4A6, Canada
[8]Division of Cell Matrix Biology and Regenerative Medicine, Faculty of Biology, Medicine and Health, University of Manchester, Manchester M13 9PL, UK
[9]Human Anatomy Unit, Department of Public Health, Experimental and Forensic Medicine, University of Pavia, 27100 Pavia, Italy
[10]These authors contributed equally
[11]Lead Contact
*Correspondence: maurilio.sampaolesi@kuleuven.be
https://doi.org/10.1016/j.celrep.2020.107597

SUMMARY

Fibrosis and fat replacement in skeletal muscle are major complications that lead to a loss of mobility in chronic muscle disorders, such as muscular dystrophy. However, the *in vivo* properties of adipogenic stem and precursor cells remain unclear, mainly due to the high cell heterogeneity in skeletal muscles. Here, we use single-cell RNA sequencing to decomplexify interstitial cell populations in healthy and dystrophic skeletal muscles. We identify an interstitial CD142-positive cell population in mice and humans that is responsible for the inhibition of adipogenesis through GDF10 secretion. Furthermore, we show that the interstitial cell composition is completely altered in muscular dystrophy, with a near absence of CD142-positive cells. The identification of these adipo-regulatory cells in the skeletal muscle aids our understanding of the aberrant fat deposition in muscular dystrophy, paving the way for treatments that could counteract degeneration in patients with muscular dystrophy.

INTRODUCTION

The skeletal muscle exists out of muscle fibers, multinucleated contractile units that are structured in bundles or fascicles, surrounded by connective tissue, also called the interstitium (Frontera and Ochala, 2015). Upon acute injury, progenitors swiftly activate their repair mechanisms and completely regenerate the skeletal muscle in a time span of weeks (Woszczyna and Rando, 2018). An abundant assembly of cells has been reported to be involved in this repair process, of which muscle satellite cells (MuSCs) are the predominant cell type (Sacco et al., 2008). MuSCs are skeletal muscle stem cells located beneath the basal lamina of muscle fibers (Mauro, 1961). In homeostatic conditions, they remain quiescent, although upon injury they proliferate, differentiate, and fuse into new or existing myofibers (Feige et al., 2018). Besides MuSCs, fibro/adipogenic progenitors (FAPs) (Joe et al., 2010), mesenchymal progenitors (Uezumi

et al., 2010), mesoangioblasts (MABs) (Dellavalle et al., 2007), Pw1+/Pax7+ interstitial cells (PICs) (Mitchell et al., 2010), and TWIST2+ progenitors (Liu et al., 2017a) have been reported as stem cell populations that directly or indirectly support myogenic regeneration. However, the current characterization of these cells does not suffice, as many of these cell types share overlapping markers and functions.

In chronic injury, regeneration deteriorates, leading to increased adipogenesis and fibrosis at the expense of the muscle fibers (Hamrick et al., 2016; Mann et al., 2011). This deposition of fat and extracellular matrix (ECM) leads to progressive muscle weakening and dysfunction, leading to the loss of ambulation and respiratory complications (Mercuri and Muntoni, 2013). Although the mechanisms of fibrosis in muscular dystrophy are generally understood (Joe et al., 2010; Lemos et al., 2015; Mueller et al., 2016; Uezumi et al., 2011), it is still unclear how adipogenesis arises in chronic muscle regeneration. FAPs

are described as the main players (Joe et al., 2010; Uezumi et al., 2011), although it has been shown that MuSCs are also able to participate in adipogenesis (Pasut et al., 2016). Most studies aimed at understanding muscle adipogenesis through extended molecular characterization of the resident cell types in physiological and pathological conditions. However, current methods using bulk-cell populations isolated based on a small set of surface markers are limited in resolving the heterogeneity, niche specificity, and complexity of interstitial cell types within the skeletal muscle (Costamagna et al., 2015; Pannérec et al., 2013; Wosczyna and Rando, 2018). Single-cell technology allows for unbiased characterization of skeletal muscle cell types as well as their transition from a healthy to a diseased state.

Despite the wealth of information, it is still not well understood how cell types in skeletal muscle cope with chronic injury and how they switch toward an adipogenic phenotype. Importantly, the cell types that play a role in disease progression are numerous, and their specific involvements remain controversial. Here, we combine unbiased single-cell RNA sequencing, extensive cell fate characterization, genetic perturbation, and computational modeling to comprehensively characterize the alteration of the interstitial landscape in the skeletal muscle exposed to chronic injury. Using a mouse model of limb-girdle muscular dystrophy (LGMD) that closely resembles symptoms of human skeletal muscle deterioration (Durbeej et al., 2000), we uncovered an interstitial cell subpopulation in the SCA-1 and PDGFRA-positive population that controls adipogenesis in the skeletal muscle. Further analysis showed that this population is also present in healthy human skeletal muscle and that its presence is drastically decreased in dystrophic muscle. Upon isolation of this cell type, we found that this population controls adipogenesis in a cell-number-dependent manner. Furthermore, dystrophic muscle showed a reduced number of CD142$^+$ cells compared to healthy muscle, resulting in an increased adipogenic differentiation of the SCA-1$^+$ cells. Knockdown and overexpression of *Gdf10* showed the importance of this paracrine mediator in the blocking of adipogenesis by CD142$^+$ cells. Lastly, *in vivo* absence of GDF10 led to an increased adipogenesis in the skeletal muscle that exacerbated upon injury. Overall, our study identified an adipo-regulatory cell (Areg) in the skeletal muscle and portrays its importance in sustaining skeletal muscle function by providing evidence that this population is absent in chronic muscle injuries, such as LGMD, due to pathological remodeling of the interstitial landscape.

RESULTS

Single-Cell RNA Sequencing Resolves the Skeletal Muscle Interstitial Heterogeneity

To molecularly characterize intra-muscular fat deposition and the responsible stem cell populations, we performed unbiased single-cell RNA sequencing (scRNA-seq) from the hindlimbs of C57Bl6 (healthy) and *Sgcb*-null (dystrophic) mice (Figures 1A and S1A). Endothelial and hematopoietic cells were excluded through sorting of LIN$^-$(CD31$^-$CD45$^-$TER119$^-$) cells. After thorough quality control, we retained 256 high-quality cells (Figures S1B and S1C) and confirmed the effectiveness of our sorting

strategy by showing that all cells were negative for endothelial and hematopoietic markers (Figure S1D). Clustering resulted in seven groups that were annotated as MuSCs, smooth muscle cells (SMCs), Schwann cells, fibroblasts, and three clusters of interstitial stromal cells (ISCs) (Figures 1B and S1E–S1G). Every cluster was characterized by the expression of marker genes like *Fmod* and *Tnmd* for fibroblasts (Westergren-Thorsson et al., 1991; Yamana et al., 2001), *Myl9* and *Tpm2* for smooth muscle cells (Dube et al., 2014; Licht et al., 2010), *Myf5* and *Cd82* for MuSCs (Alexander et al., 2016; Nervi et al., 1995), *Plp1* and *Sox10* for Schwann cells (Kuhlbrodt et al., 1998; Nave et al., 1987), and the co-expression of *Ly6a*, *Pdgfra*, and *Cd34* for ISCs (Figures 1C and 1D; Table S1). Furthermore, we checked the validity of common marker genes and proposed improved markers for these populations in the skeletal muscle (Figure S1H). Checking the top area under the receiving operator curve (AUROC) showed us that *Cd82* and *Fgfr4* are better markers for MuSCs than *Desmin* and *Myf5* (Figure S1H). CD82 has already shown to be an excellent marker for human satellite cells (Alexander et al., 2016).

The ISCs subclustered into three groups, which demonstrates the heterogeneity of this population (Figures 1C and 1D). Every ISC population expressed specific markers, like *Ly6c1* and *Cd55* for ISC 1, *Gdf10* and *Meox2* for ISC 2, and *Thbs4* and *Fbln7* for ISC 3. The latter markers were also observed in the fibroblast population (Figure 1D). ISC 1 had the highest expression of the stem-cell-related genes *Ly6a* and *Cd34*. In addition, gene set enrichment analysis revealed signaling pathways, such as transforming growth factor β (TGF-β) and Wnt, and a high correlation to blood vessels and adipose tissue (Figures 1D, 1E, and S1I; Table S2). ISC 2 correlated to TGF-β regulators and Wnt signaling pathways and was linked to blood vessels (Figure S1I). ISC 3 was highly enriched for ECM organization and metallopeptidase activity and is linked to skin tissue (Figure S1I).

Recently, the Tabula Muris Consortium (Schaum et al., 2018) and Giordani et al. (2019) published scRNA-seq data of mouse limb muscle based on the 10X Genomics platform. By comparing sequencing metrics, we found that our dataset was sequenced with more depth and detected more than double the number of genes compared to the other datasets (Figure S2A). Raw counts were retrieved for the Giordani data (n = 12,441); therefore, we reannotated the cell types based on their annotation (Figure S2B). We were able to retrieve all clusters plus three small unannotated clusters that we named after their top DE marker (Figure S2C). In addition, the Schaum data for hindlimb muscles (n = 4,543) were filtered and reanalyzed, although here, cluster names were already provided by the authors (Figure S2D). To compare the validity of our clusters, we measured the percentage of matched cell type markers (STAR Methods) between our data and the Giordani (Figure S2E) and Schaum dataset (Figure S2F). Data integration showed that all datasets smoothly overlapped and no specific dataset clusters arose (Figure S2G). As all our cell clusters overlapped with clusters of the public data (Figure S2H), we could label all clusters accordingly (Figure S2I). In summary, we performed scRNA-seq on healthy and dystrophic skeletal muscle and identified five cell types, which were validated in public
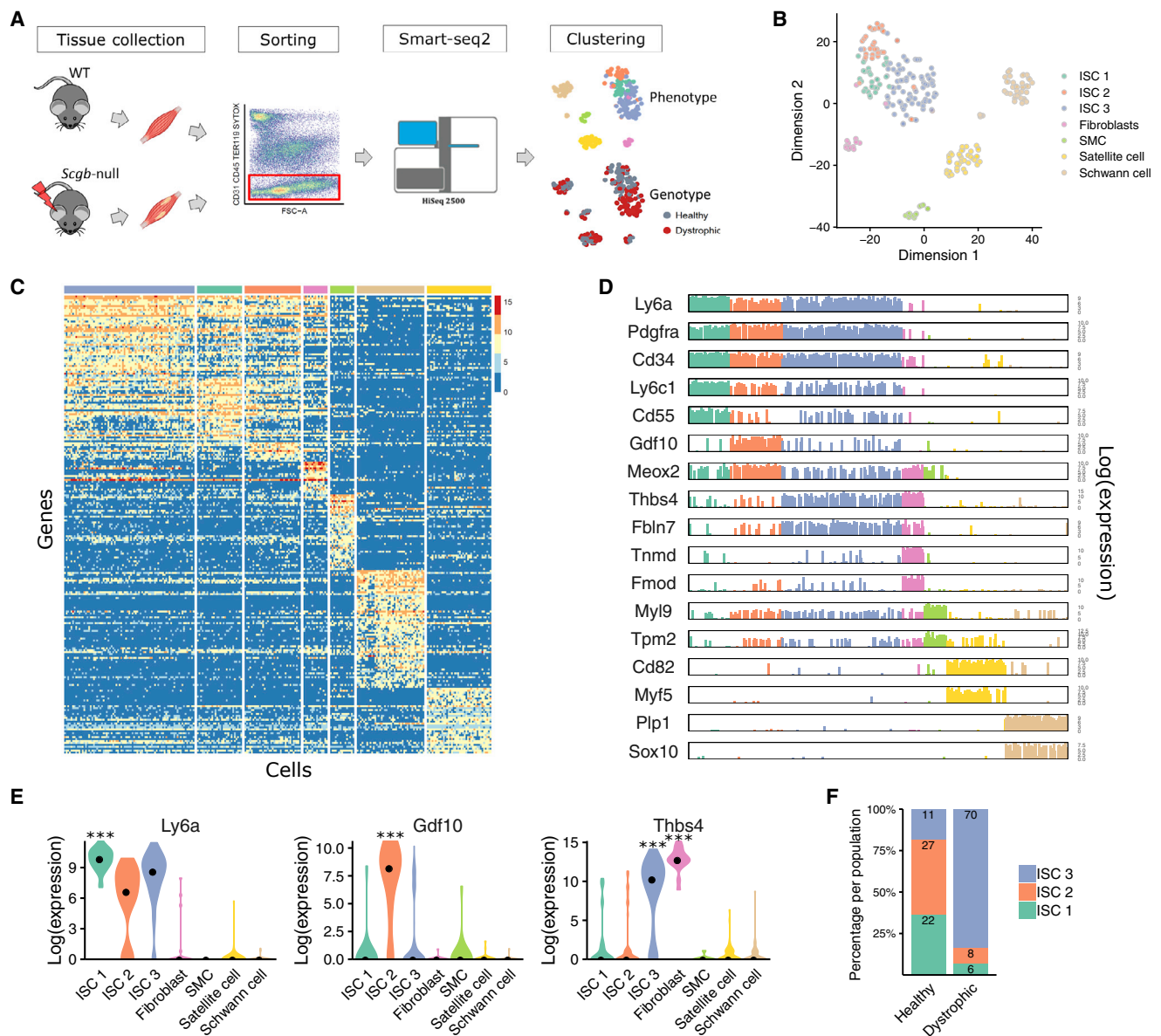
Figure 1. Single-Cell RNA Sequencing Reveals the Cellular Heterogeneity in Healthy and Dystrophic Skeletal Muscle

(A) Schematic diagram showing the isolation of single cells from the hindlimbs of healthy and dystrophic mice with SMART-seq2.

(B) t-SNE plot and *k*-means clustering of 256 cells from healthy and dystrophic skeletal muscle. Every point represents one cell.

(C and D) Heatmap of k-means clusters with 237 marker genes (C). Bar plot showing the expression level (log-normalized counts) of selected marker genes (D).

(E) Violin plot with median visualizing marker genes for ISC clusters. The expression is shown as log-normalized counts. ***p ≤ 0.001.

(F) Bar plot showing the percentage of ISC clusters in healthy and dystrophic skeletal muscle.

See also Figures S1 and S2 and Tables S1 and S2.

scRNA-seq data. In addition, we observed a distinction of ISCs into three clusters.

A Dystrophy-Specific Activated Satellite Cell Cluster

To check how cell types adapt to muscular dystrophy, we examined whether any clusters were enriched for a specific genotype (Figures S1J and S1K). The most striking difference between healthy and dystrophic cells was found in the ISCs. Although ISC 1 and 2 are mainly present in healthy muscle, ISC 3 domi-

nates in dystrophic muscle (Figure 1K). Surprisingly, we did not find obvious changes in the MuSCs. Nevertheless, when we clustered MuSCs separately, we found that they group according to different differentiation stages (Figure S3A; Table S3). Despite the limited number of cells (n = 40), we identified a cluster of quiescent and activated MuSCs, as well as myoblasts through the expression of essential myogenic transcription factors *Pax7*, *Myf5*, *Myod1*, and *Myog* and through pseudotemporal ordering (Figures S3B and S3C). Furthermore, we found

a cluster of activated MuSCs that was only present in the dystrophic muscle. This group of dystrophic activated MuSCs expressed unique markers, such as *Angptl4*, *Arhgap5*, *Grsf1*, and *Dpysl3* (Figure S3D). Many of these genes are linked to lipid metabolism and cytoskeletal remodeling (Aryal et al., 2016; Hinge et al., 2017). We checked these genes in the satellite cell cluster of the Tabula Muris Consortium dataset and could confirm that, in healthy satellite cells, these genes are rarely expressed (Figures S3E and S3F). Nevertheless, additional experiments are necessary to verify whether this population is present in muscular dystrophy and what its effect is on satellite cell differentiation.

Projection of Known Interstitial Progenitor Markers

To check the presence of previously identified progenitor populations, we checked the expression of their key markers in our clusters: *Ly6a* for FAP (Joe et al., 2010); *Pdgfra* for mesenchymal progenitors (Uezumi et al., 2010); *Alpl* for MABs (Dellavalle et al., 2007); and *Peg3* or *Pw1* for PICs (Mitchell et al., 2010). Except for *Peg3*, we found that all markers were located only within the ISC clusters (Figures 2A and 2B). *Ly6a* was mainly expressed in ISC 1, although ISC 2 had a higher expression of *Pdgfra*. Furthermore, *Alpl* was limited to ISC 2 and ISC 3, although the expression of *Peg3* increased from ISC 1 to ISC 3, which could implicate that it plays a more important role in muscular dystrophy (Figure 2C; Table S3).

Because we could not connect these progenitors to a specific ISC cluster, we asked whether these cell types are functionally distinct. Therefore, we sorted MABs as LIN⁻ALPL⁺ and FAPs as LIN⁻SCA-1⁺ cells and subjected them to a co-culture together with freshly isolated MuSCs to check their myogenic potential. We found that both MABs and FAPs possess the ability to fuse with MuSCs (Figure 2D). In addition, because these progenitors are known to be multipotent, we checked for adipogenic differentiation potential and did not find any differences in their potency to differentiate toward adipocytes (Figure 2E).

Although MABs and FAPs are transcriptionally not as distinct from each other as previously thought, we nonetheless wanted to assess the possibility of a hybrid transition phase between these markers during muscle development. Therefore, we checked whether MABs could become FAPs by lineage tracing with a tamoxifen-inducible Cre-lox system under the *Alpl* promoter (Dellavalle et al., 2007). By fluorescence-activated cell sorting (FACS) analysis for Alpl-YFP, we showed that the percentage of SCA-1 in ALPL⁺ cells increases over age (Figures S3G and S3H). This suggests that, upon the development of the skeletal muscle, there is a tight connection between MABs and FAPs. In summary, we show that four specific markers for previously reported progenitor populations—although being expressed at different levels—are not allocated to a specific cluster and that MABs and FAPs share similar differentiation potential *in vitro* and *in vivo*.

ISC Dynamics in Muscular Dystrophy

Because ISC 1, ISC 2, and ISC 3 did not specifically relate to any predefined muscle stem cell population, we wanted to determine the distinction that exists between these clusters.

A first distinction of heterogeneity was observed in *Vcam1* and *Tek* expression. Although *Vcam1* is expressed in ISC 2 and ISC 3, *Tek* is exclusively expressed in ISC 1 (Figures S4A and S4B). As this does not explain the difference between ISC 2 and ISC 3, we selected all cells defined as ISC 1, ISC 2, and ISC 3 and performed clustering after quality control to get rid of technical variability due to External RNA Controls Consortium (ERCC) levels (Figure S4C). We could find five clusters, supported by a consensus plot, silhouette plot, and the stability index (Figures S4D–S4F). All cells maintained the same annotation that was observed in clustering of all LIN⁻ cells (Figure S4G). We found that ISC 3 consists of three different subgroups: ISC 3a; ISC 3b; and ISC 3c (Figure 3A). The ISC 3 clusters expressed variability in ISC 3 markers, such as *Thbs4*. Furthermore, specific markers were expressed per cluster, such as *G0s2* for ISC 3a, *Ptx3* for ISC 3b, and *Cthrc1* for ISC 3c (Figure 3B; Table S4). The markers PTX3 and CTHRC1 were validated through immunofluorescent staining of healthy and dystrophic skeletal muscle, observing a drastic increase of both markers in dystrophic mice (Figures 3C–3F).

Considering that we observed a fractional increase in expression of specific ISC 3 markers and a smooth transition in genotype from ISC 1 to ISC 3c (Figure S4H), we wondered whether the ISC clusters we observed are transitional states. Therefore, we build single-cell trajectories that show three branches, each belonging to an ISC type. We can observe ISC 1, ISC 2, and ISC 3c at the ends of their respective branches, although ISC 3a and 3b are intermittent (Figure 3G). Ordering these trajectories in pseudotime showed a conversion from ISC 1 and ISC 2 to ISC 3a and ISC 3b, with ISC 3c as the end state (Figure S4I). RNA velocity analysis confirmed the direction from ISC 1 and ISC 2 to ISC 3 (Figure 3H). Through branched expression analysis modeling (BEAM) analysis, four-gene cluster could be identified that showed high variability between these cell states (Figure S4J). Here, several matrix metalloproteases, such as *Mmp3* and *Mmp14*, were found to be responsible for the transition from ISC1 to ISC3 (Figure S4K). Combined with a high expression of *Timp3* in ISC 1, our data correlated with a recent publication where TIMP3 was shown to repress injury-induced adipogenesis through inhibition of MMP14 (Kopinke et al., 2017). In addition, we found a high expression of Il6 and Arid5b in ISC 3 compared to ISC 1 (Figure S4L). Both genes are important mediators of a muscular dystrophy phenotype and adipogenesis (Liu et al., 2017b; Wada et al., 2017). We observed a major remodeling of ISC clusters between healthy and dystrophic muscle. More specifically, we saw an increase in ISC 3 in dystrophic muscle with the emergence of ISC 3c, while at the same time, ISC 1 and ISC 2 are highly reduced but still present (Figure 3I). Further, Gene Ontology (GO) analysis showed that ISC 3b is enriched for lipid storage and localization—and in general relates the most to adipose tissue—although ISC 3c relates to wound healing and ECM assembly and is highly correlated to skin tissue (Figure S4M; Table S5). However, we would like to highlight that, in order to confirm our pseudotime results, lineage-tracing studies should be performed to prove the conversion from ISC 1 to ISC 3.
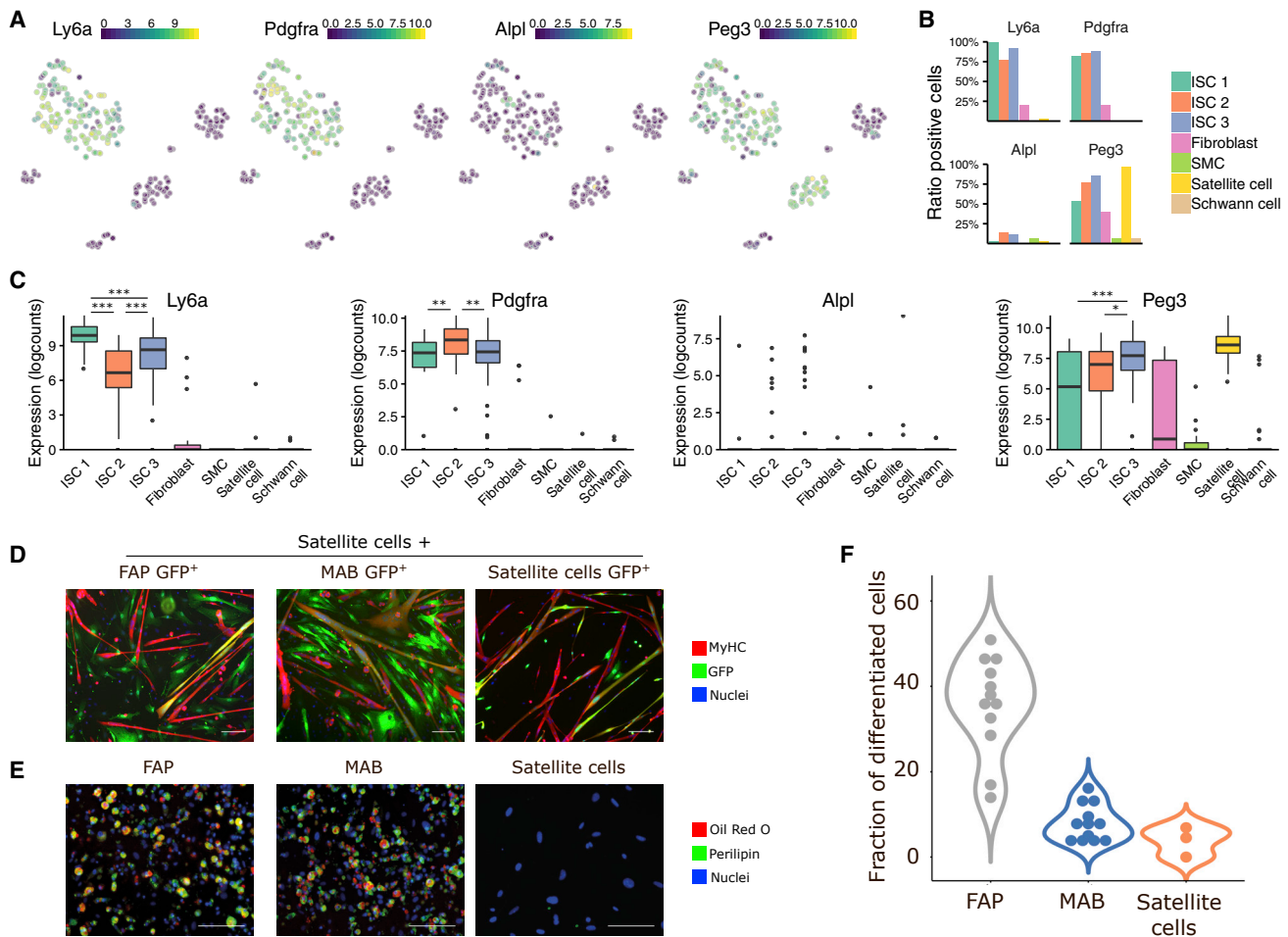
Figure 2. Most Interstitial Stem Cell Markers Are Localized in One Large Interstitial Stem Cell Cluster

(A–C) Expression of stem cell marker genes.

(A) t-SNE plot of healthy and dystrophic skeletal muscle. Every point represents one cell. Gene expression is shown as log-normalized counts.

(B) Bar plot of the number of cells per cluster positive for genes shown in (A).

(C) Boxplot per cluster. *$p \leq 0.05$; **$p \leq 0.01$; ***$p \leq 0.001$.

(D) Microscopy images of myogenic differentiation in co-culture with MuSCs and GFP+ MABs and GFP+ FAPs. Myotubes stained with MyHC (red), MABs, FAPs stained with GFP (green), and nuclei stained with Hoechst 33258 (blue) are shown.

(E) Microscopy images of adipogenic differentiation from MABs (ALPL+), FAPs (SCA-1+), and MuSCs. Adipocytes are stained with Oil Red O (red) and PERILIPIN-1 (green), and nuclei are stained with Hoechst 33258 (blue).

(F) Fraction of differentiated cells per population shown in (E) (n = 12). Data are represented as mean ± SEM.

Scale bars, 50 μm. See also Figure S3 and Table S3.

Because our scRNA-seq data are made up out of healthy and dystrophic cells, we wanted to make sure that genotype did not have an influence on clustering of the ISCs. Therefore, we regressed out the genotype and reanalyzed the data. In low dimensionality, we can observe that all ISC clusters are still located together. For that reason, we can conclude that genotype did not influence clustering (Figure S5A). In addition, to make sure that the ISC clusters we found are generally present in mouse limb muscle, we integrated "FAPs" of the Giordani data (n = 1,517) and "mesenchymal stem cells" of the Schaum data (n = 1,127) together with our ISC data and observed perfect overlap between the datasets (Figure S5B). ISC clusters still localized together, which is also shown by the expression of

typical marker genes (Figures S5C and S5D). We reclustered the data and were able to find clusters relating to ISC 1, ISC 2, ISC 3a, and ISC 3b, although we did not find a cluster relating to ISC 3c, which is expected because this cluster was specific to dystrophic muscle (Figure S5E). In addition, there was one ISC cluster that we did not find in our data as well as two more distinct clusters: one we annotated as SCA-1 negative and the other one as endothelial-like (Figure S5E). We checked the presence of cells from every dataset per cluster and were able to observe cells from our dataset in the unannotated cluster (Figures S5F and S5G). This is most likely because of the low number of cells in our dataset. In summary, we showed that ISC 3 consists of three subtypes, all of which express subtype-specific
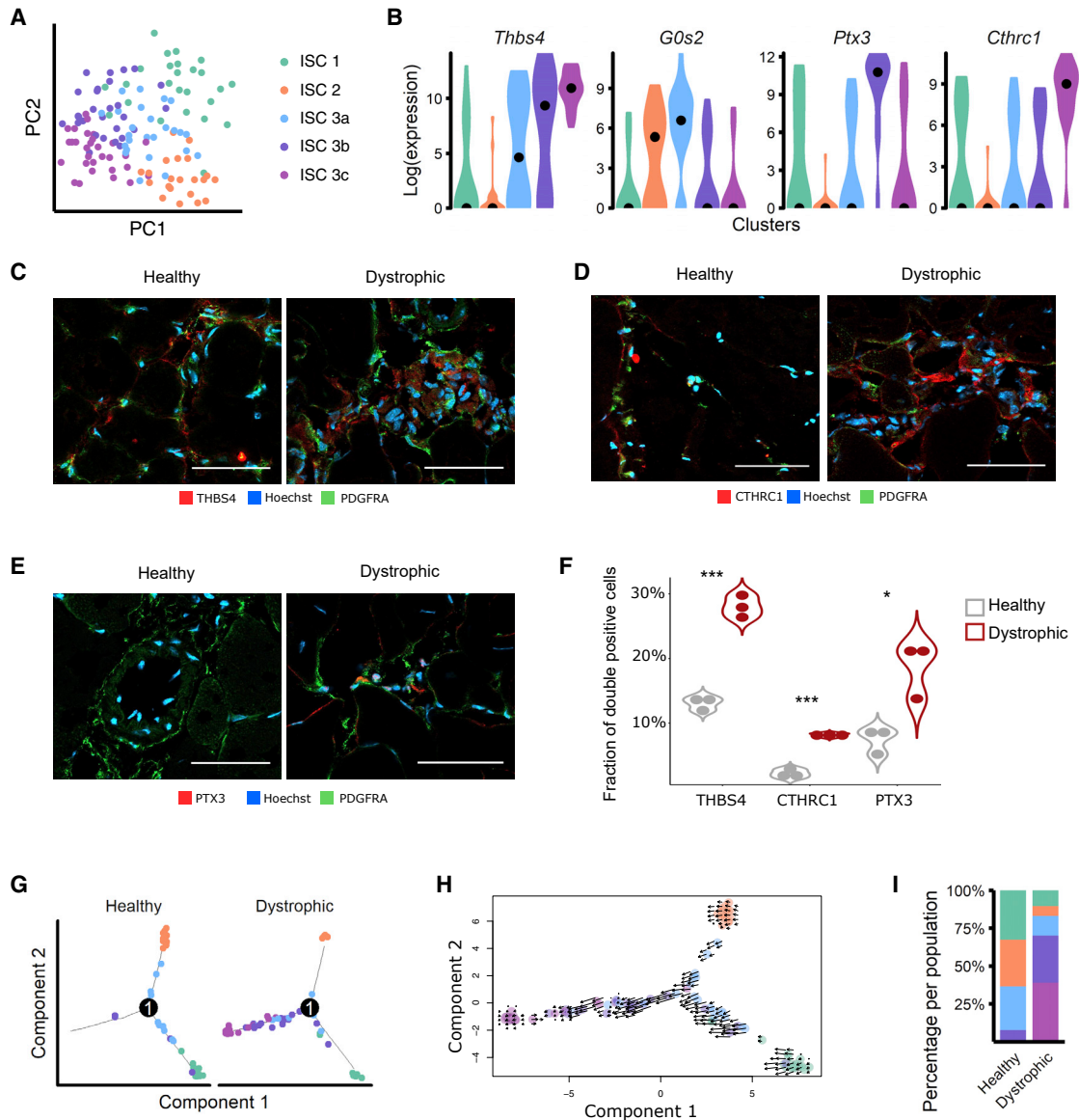
Figure 3. Different ISC Subtypes Arise in Muscular Dystrophy

(A) PCA plot and *k*-means clustering (*k* = 5) of 125 ISCs. Every point represents a cell as ISC.

(B) Violin plot visualizing the expression of marker genes per ISC 3 cluster plotted. Expression is shown as log-normalized counts together with the median.

(C–E) Microscopy images of the skeletal muscle of healthy and dystrophic mice. ISCs are stained for PDGFRA (red), Hoechst 33258 (blue), and THBS4 (C), CTHRC1(D), and PTX3 (E; all in green).

(F) Fraction of PDGFRA-positive cells that are THBS4, CTHRC1, and PTX3 positive in healthy and dystrophic mice (mean ± SEM).

(G) Minimum spanning tree of healthy and dystrophic ISCs based on the expression pattern of 1,000 genes with the first two dimensions of PCA on *k*-means clusters (*k* = 5). Each point represents one cell; the solid black line represents the pseudotime ordering. Cells are colored based on *k*-means clustering from (A).

(H) Observed and extrapolated future cell states (arrows) are shown using Gaussian smoothing on a regular grid on the first two Monocle components from (G). RNA velocity was estimated without cell or gene pooling. Cells are colored based on *k*-means clusters from (A).

(I) Bar plot showing the percentage of each ISC cluster in healthy and dystrophic muscle.

Scale bars, 50 μm. *p ≤ 0.05; ***p ≤ 0.001. See also Figures S4 and S5 and Tables S4 and S5.

marker genes and are also present in other public datasets. Moreover, we showed that these subtypes likely transition from ISC 1 and ISC 2 to ISC 3 and that, in muscular dystrophy, an ISC 3c population arises.

Identification of an Interstitial Population that Controls Adipogenesis

As these ISC groups did not relate to markers of dedicated progenitor populations, we questioned whether there is an
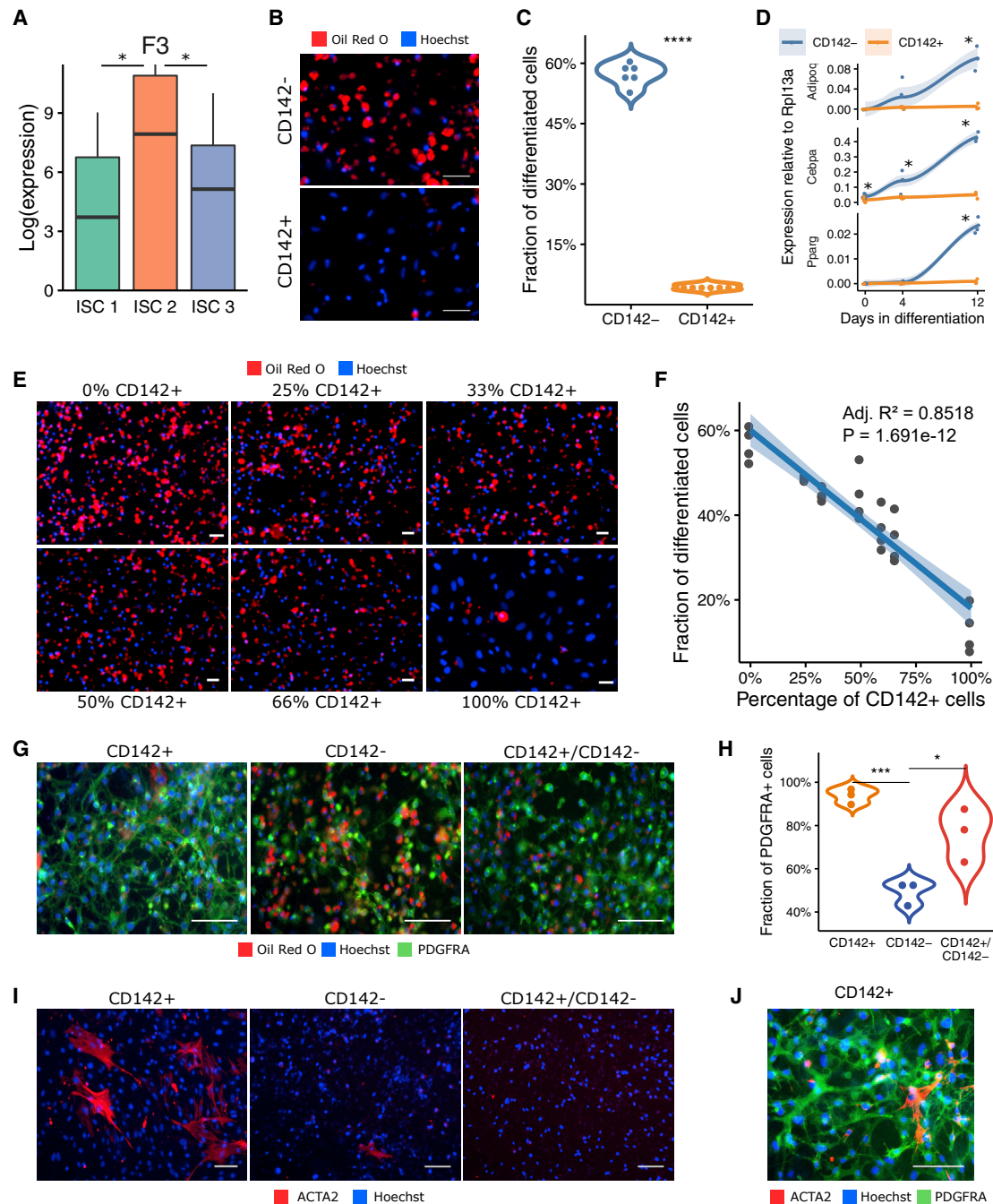
Figure 4. CD142$^+$ ISCs Inhibit Adipogenesis

(A) Expression of *F3* (CD142) assessed by scRNA-seq. *p ≤ 0.05.

(B) Microscopy images of CD142$^-$ and CD142$^+$ after the induction of adipogenesis.

(C) Fraction of differentiated cells per population shown in (B) (n = 6).

(D) qPCR analysis of key adipogenic transcription factors during adipogenesis. Expression is relative to *Rpl13a.* Loess curve is fitted through data points; uncertainty is displayed as 95% confidence interval (n = 3).

(E) Microscopy images of transwell assays with distinct ratios of CD142$^-$ (bottom) and CD142$^+$ ISCs (top).

(F) Fraction of differentiated cells per ratio in (E) (n = 4).

(G) Microscopy images of transwell assays stained for Oil Red O (red) and PDGFRA (green).

(H) Fraction of PDGFRA$^+$ cells per population shown in (G) (mean ± SEM; n = 3).

(legend continued on next page)

adipogenic function linked to any of the ISC clusters. Recently, a cell population has been discovered in fat depots that inhibits adipogenesis (Schwalie et al., 2018). These Aregs comprise a population inside LIN⁻SCA-1⁺ cells from subcutaneous stromal vascular fractions. By comparing the top 200 marker genes, we found striking similarities, especially for ISC 1 and ISC 2 (Figure S6A). In addition, we could observe adipogenic genes, *Pparg* and *Fabp4*, in every ISC cluster except for ISC 2 (Figure S6B). We sorted these populations based on selected marker genes: *Cd55* for ISC 1; *F3* (encoding CD142) for ISC 2; and *Sdc1* for ISC 3 (Figures 4A and S6C). We were able to sort for CD55 and CD142, however, not for SDC1 (Figure S6D; data not shown). When we subjected these sorted cell populations to an adipogenic differentiation assay *in vitro*, we observed a lack of adipogenic response from CD142⁺ ISCs, although CD142⁻ ISCs showed an increased adipogenic response compared to bulk ISCs (Figures 4B and 4C). Furthermore, CD55⁺ ISCs showed a high adipogenic response, although the adipogenic capacity of CD55⁻ ISCs was lower compared to bulk ISCs (Figures S6E and S6F). These observations were confirmed by qPCR analysis of adipogenic genes (Figures 4D and S6G). Because of the opposite effects in adipogenesis that we observe between CD142⁺ and CD55⁺ ISCs, we hypothesized that CD142⁺ ISCs inhibit adipogenesis. To validate this hypothesis, we conducted a titration experiment, seeding CD142⁻ ISCs at the bottom and CD142⁺ ISCs at the top of a transwell plate in different ratios. We observed a negative linear relationship between adipogenesis in CD142⁻ ISCs and the amount of CD142⁺ ISCs (Figures 4E and 4F). Thus, we can conclude that we found compelling evidence for the existence of Aregs in the murine skeletal muscle.

Next, we wanted to know whether the CD142⁺ cells kept the CD142⁻ ISCs in their progenitor state or pushed them toward another cell fate. Therefore, we performed an adipogenic differentiation of CD142⁻, CD142⁺, and a transwell assay, seeding CD142⁻ ISCs (bottom) and CD142⁺ ISCs (top). After differentiation, practically all CD142⁺ cells remained positive for PDGFRA, although CD142⁻ ISCs, which differentiate to adipocytes, became negative for PDGFRA (Figures 4G and 4H). When CD142⁻ and CD142⁺ ISCs were incubated together, we could clearly observe a decrease in adipocytes and an increase in PDGFRA⁺ cells, marking progenitors (Figures 4G and 4H). In addition, we could find a small number of α-smooth muscle actin (ACTA2)⁺ cells, marking fibroblasts, mostly in the CD142⁺ population (Figure 4I). These cells lost PDGFRA expression during differentiation (Figure 4J). From these results, we can conclude that, upon adipogenic differentiation, CD142⁺ ISCs stayed nearly all PDGFRA⁺—although a small fraction becomes positive for ACTA2—and that, when incubated with CD142⁻ ISCs, they are kept in a progenitor state.

A Deficiency of Adipo-regulatory Cells in Dystrophic Muscle Is Directly Proportional to an Increased Adipogenesis

Based on our scRNA-seq data, we found a vast reduction of Aregs in dystrophic muscle. Therefore, we wondered whether this results in an increased adipogenic potency of dystrophic ISCs. Therefore, we isolated bulk ISCs (LIN⁻PDGFRA⁺SCA-1⁺), CD142⁺ ISCs, and CD142⁻ ISCs from the skeletal muscle of healthy and dystrophic mice (Figures 5A and 5B). We could validate the findings from our scRNA-seq experiment, as there was a significantly lower number of CD142⁺ ISCs in dystrophic mice (Figure 5C), and we observed an increased adipogenic propensity in bulk dystrophic ISCs compared to healthy ISCs. However, this difference was completely abolished when CD142⁻ ISCs and CD142⁺ ISCs were separated (Figures 5D and 5E). Therefore, we conclude that the increased adipogenic potency of ISCs from dystrophic muscle is linked to the decreased ratio of CD142⁺/CD142⁻ ISCs that is present in the skeletal muscle of *Sgcb*-null mice.

To find out whether Aregs are not only restricted to murine skeletal muscle, we isolated CD142⁺ and LIN⁻ ISCs from human skeletal muscle biopsies of healthy and dystrophic patients. Like in murine muscle, we observed a lower number of CD142⁺ ISCs in the samples of dystrophic patients, compared to healthy muscle biopsies (Figure 5F). Transwell assays with CD142⁺ and CD142⁻ ISCs incubated together with healthy and dystrophic muscle in the insert resulted in an increased adipogenesis in CD142⁻ ISCs compared to CD142⁺ ISCs (Figures 5G, 5H, and S6H–S6J). In addition, we also tested the myogenic commitment of human CD55⁺ ISCs and found that these cells showed a higher myogenic propensity compared to the CD55⁻ ISCs *in vitro* and *in vivo* (Figures S6K and S6L). In summary, we show that Aregs and CD55⁺ ISCs are present in human skeletal muscle and are functionally similar to their murine equivalent.

Aregs Suppress Adipogenesis via GDF10

To resolve the mechanism by which Aregs exert their adipogenic inhibition, our interest fell upon *Gdf10*, one of the highest-expressed markers of this population (Figure 6A). In addition, we found that *Gdf10* expression increased up to 5-fold in CD142⁺ ISCs during adipogenic differentiation (Figure 6B). We subjected CD142⁺ ISCs to small interfering RNA (siRNA)-mediated *Gdf10* reduction, lowering the expression of *Gdf10* (Figure S7A) without affecting cell viability (Figures S7B and S7C). A transwell assay was performed with CD142⁻ ISCs (bottom) and *Gdf10*-silenced or scramble control CD142⁺ ISCs (top). Here, we observed an increased adipogenesis of CD142⁻ ISCs that were incubated together with *Gdf10*-silenced CD142⁺ ISCs compared to scramble control (Figures 6C and 6D). In addition, overexpressing *Gdf10* in CD142⁻ ISCs (Figures S7D and S7E) resulted in a decrease of adipogenic differentiation in CD142⁻ ISCs (Figures 6E and 6F). From these results, we can conclude that GDF10

(I) Microscopy images of transwell assays stained for ACTA2 (red) to indicate smooth muscle cells/myofibroblasts.
(J) A microscopy image of transwell assays stained for ACTA2 (red) and PDGFRA (green). Scale bars, 50 μm (B and E) and 100 μm (G, I, and J). *p ≤ 0.05; ***p ≤ 0.001. See also Figure S6.
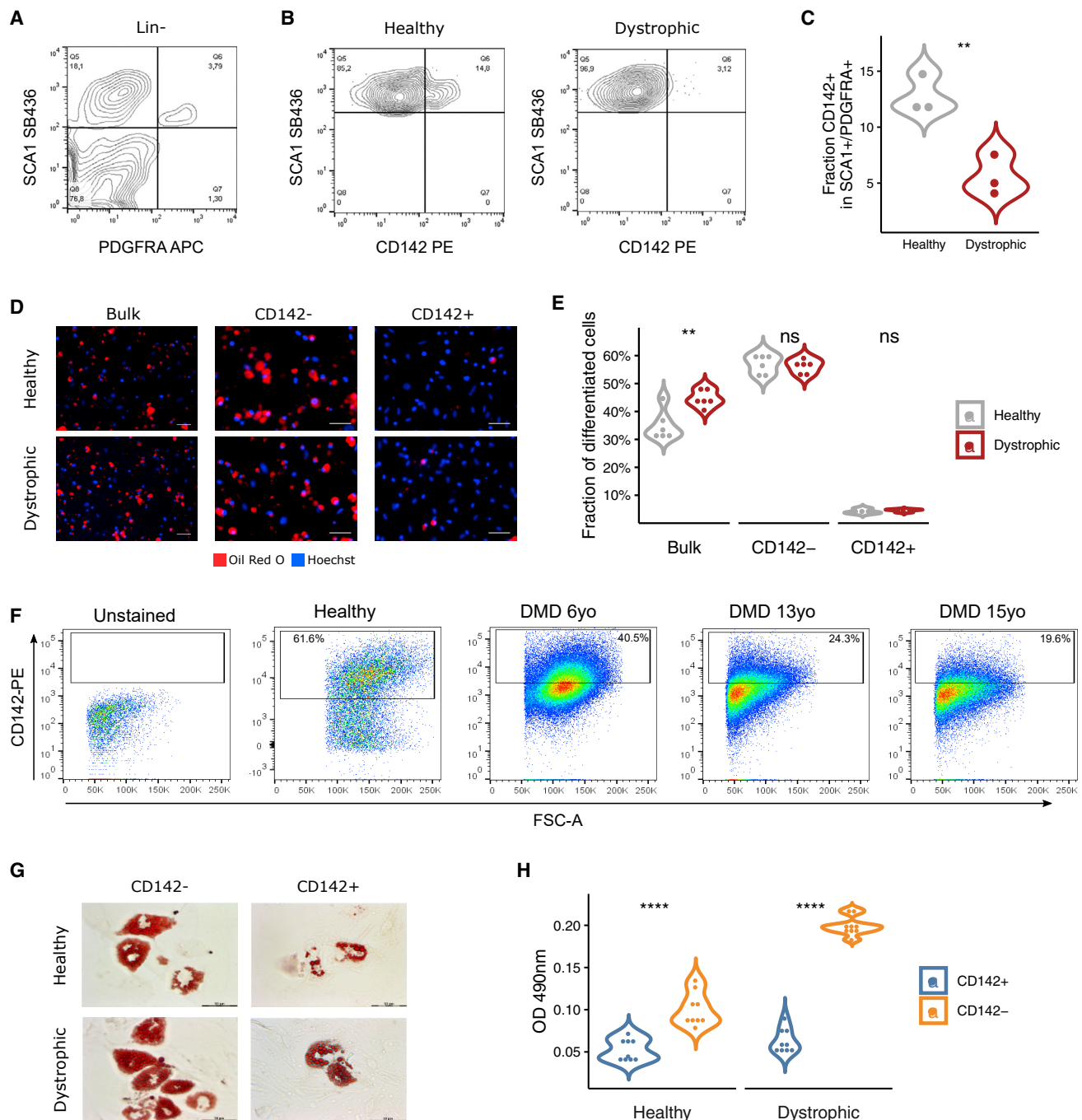
Figure 5. Dystrophic ISCs Possess an Increased Adipogenic Potency due to a Deficit of CD142+ ISCs

(A and B) FACS-based sorting strategy to isolate bulk (LIN−SCA-1+; A), CD142−, and CD142+ ISCs isolated from healthy and dystrophic mice (B).

(C) Fraction of CD142+ ISCs shown in (B) (n = 3).

(D) Microscopy images of bulk, CD142−, and CD142+ ISCs isolated from healthy and dystrophic mice after the induction of adipogenesis. Nuclei are stained with Hoechst 33258 (blue), and lipids are stained with Oil Red O (red).

(E) Fraction of differentiated cells per population shown in (D) (n = 6).

(F) FACS analysis of the CD142+ fraction of LIN−(CD45−, CD31−, CD119−) skeletal muscle cells from a healthy donor and a 6-, 13-, and 15-year-old patient with Duchenne muscular dystrophy.

(G) Microscopy images of transwell assays with human CD142− and CD142+ cells (bottom) incubated with healthy or dystrophic muscle (top). Lipids are stained with Oil Red O (red).

(H) Quantification of optical density at 490 nm (OD490) per population shown in (G) (n = 9).

Scale bars, 50 μm. Data are represented as mean ± SEM. **p ≤ 0.01; ****p ≤ 0.0001. See also Figure S6.

A Gdf10
B Gdf10
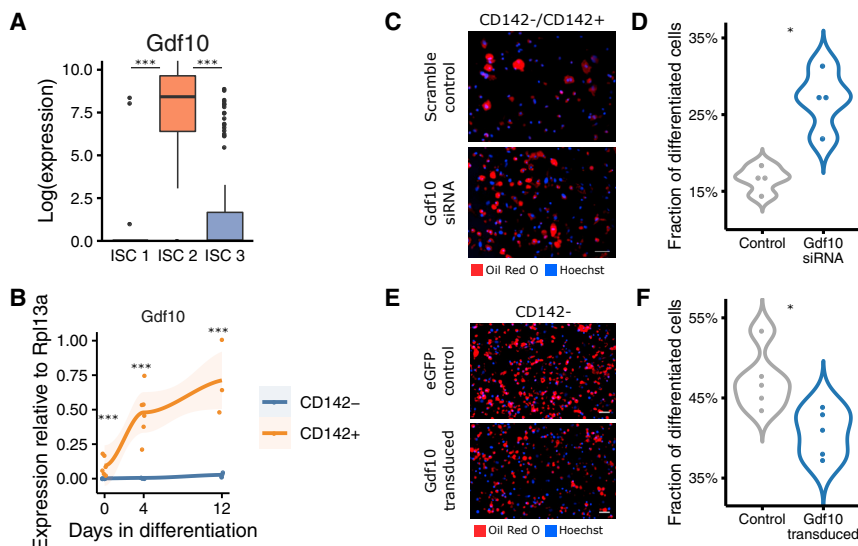**C** CD142-/CD142+
D
E CD142-
F

Figure 6. GDF10, Secreted by CD142^{+} ISCs, Is Responsible for the Suppression of Adipogenesis

(A) Expression of ISC 2 marker, *Gdf10* (*Bmp-3b*) determined by scRNA-seq (values represent log-normalized counts). ***p ≤ 0.001.

(B) Expression of *Gdf10*, relative to *Rpl13a*, in CD142^{−} and CD142^{+} ISCs during adipogenesis (n = 3–6).

(C) Microscopy images of a transwell assay with CD142^{−} ISCs (bottom) co-cultured with CD142^{+} control or Gdf10 siRNA-transfected ISCs (top) after the induction of adipogenesis.

(D) Fraction of differentiated cells per population shown in (C) (n = 4).

(E) Microscopy images after the induction of adipogenesis of CD142^{−} ISCs transduced with EGFP-control or *Gdf10*-expressing lentivirus.

(F) Fraction of differentiated cells per population shown in (E) (n = 3).

In (B), (D), and (F), t test, *p ≤ 0.05; ***p ≤ 0.001. In all panels, nuclei are stained with Hoechst 33258 (blue) and lipids are stained with Oil Red O (red). Data are represented as mean ± SEM. Scale bars, 50 μm. See also Figure S7.

plays a substantial part in the ability of skeletal muscle Aregs to suppress adipogenic differentiation.

In vivo, GDF10 is highly present in the muscle of wild-type mice although this abundance is decreased in dystrophic mice (Figure 7A). Therefore, we wanted to investigate the importance of GDF10 *in vivo*. We injured five wild-type and five *Gdf10*^{−/−} mice (Zhao et al., 1999) through a glycerol injection in the *tibialis anterior*. The contralateral leg was used as a control (saline injected). After 2 weeks, an increased fibrosis was seen upon injury, irrespective of the presence of GDF10 in the skeletal muscle (Figures 7B and 7C). However, the amount of fat deposition increased in the *Gdf10*^{−/−} compared to the wild type in both the saline- and glycerol-injected muscles (Figures 7D and 7E). This suggests that the absence of GDF10 leads to an increase of fat depots within the skeletal muscle.

DISCUSSION

Interstitial cells are frequently implicated in skeletal muscle disorders (Lemos et al., 2015; Mozzetta et al., 2013; Mueller et al., 2016; Saccone et al., 2014). However, it is still debated whether skeletal muscle regeneration is mediated only by a dedicated population of stem cells, namely MuSCs, or whether the interstitial cells actively participate to myogenesis. We and other groups provided evidence that the ISCs are therapeutically useful in stem-cell-based treatments (Judson et al., 2018; Mitchell et al., 2010; Périé et al., 2014; Sampaolesi et al., 2003, 2006). However, the use of marker-based approaches to analyze heterogeneous cell populations makes it difficult to accurately define interstitial populations. This generated a partial overlap among the different cell types in terms of shared markers and functions. In order to clarify whether these different cell types could be analogous or at different differentiation stages, there is an urgent need to distinguish the different populations of the muscle interstitium. In this direction, a recent study of singe-cell qPCR on FAPs re-

veals interesting information regarding the differential expression levels of *Tie2* and *Vcam1* in response to an acute injury or in a dystrophic environment (Malecova et al., 2018). However, the use of biased markers to isolate single cells limited the information and does not provide a full picture of the entire muscle interstitial cell composition. Another study provided clear information regarding the main cell population in healthy skeletal muscles using 10X Genomics and cytometry by time of flight (CyTOF) approaches (Giordani et al., 2019). However, it did not assess the heterogeneity of SCA-1^{+} ISCs and did not consider the consequence of pathological conditions on the cellular landscape.

Our single-cell transcriptomics-based approach overcomes many of these complications and unveils at least three populations in the interstitial progenitor pool of the skeletal muscle. Although all ISCs could be annotated as FAPs, we showed that there is more heterogeneity inside this population and that MABs belong to the ISC 2 and ISC 3 population. Furthermore, we demonstrate that there is more resemblance between these two populations as previously thought, which urges us to look differently to interstitial progenitor heterogeneity. One population that we describe consisted of CD55^{+} cells (ISC 1) that are enriched for TGF-β signaling GO terms (Table S2). ISC 1 also expressed the highest levels of stemness markers *Ly6a* and *Cd34* and retained high adipogenic potency *in vitro*. ISC 2 was characterized by *F3* and *Gdf10* expression and can block adipogenesis by paracrine signaling, of which GDF10 is an important secreted factor. It has been suggested that GDF10 acts through the TGF-β pathway in cancer cells (Upadhyay et al., 2011). Furthermore, Platko et al. (2019) showed that peroxisome proliferator-activated receptor γ (PPARγ) is antagonized by GDF10 in hepatocytes through the TGF-β/SMAD3 pathway. More research will be necessary to find out whether ISC 2 controls adipogenesis via the same mechanism. ISC 3 is a more heterogeneous population and is characterized by the
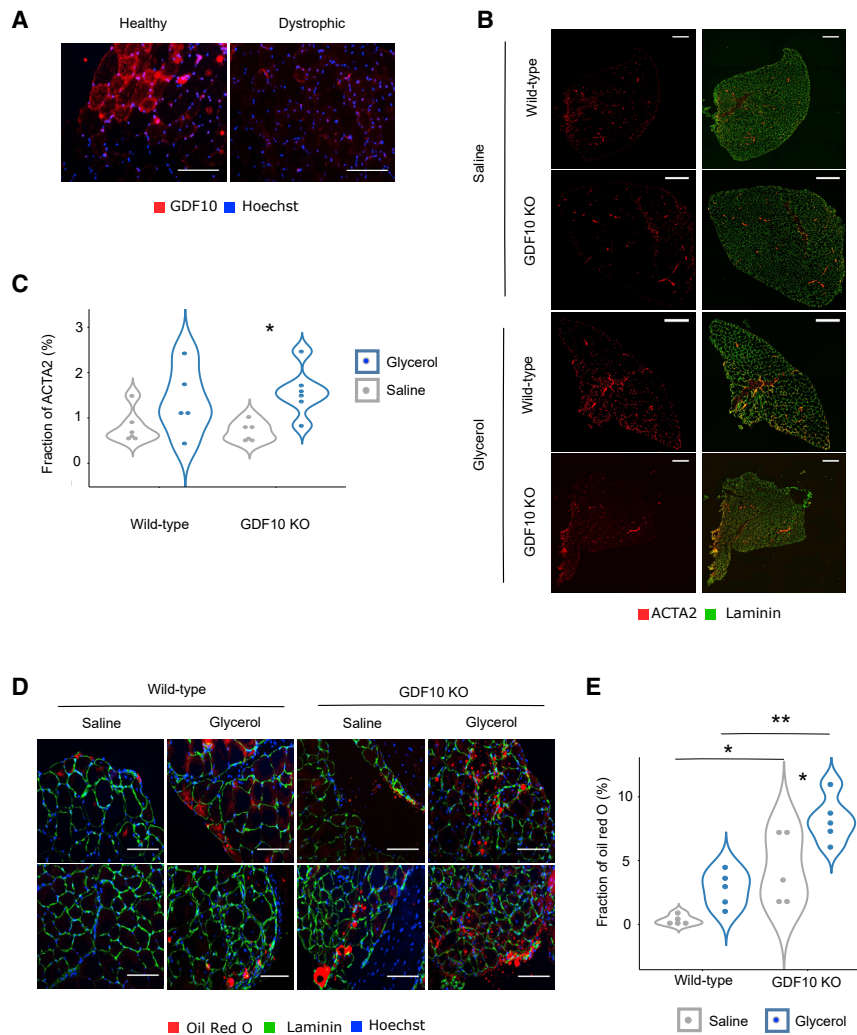
A

Healthy   Dystrophic

■ GDF10 ■ Hoechst

C

Fraction of ACTA2 (%)

*

□ Glycerol
□ Saline

Wild-type   GDF10 KO

B

Saline — Wild-type / GDF10 KO
Glycerol — Wild-type / GDF10 KO

■ ACTA2 ■ Laminin

D

Wild-type   GDF10 KO
Saline Glycerol   Saline Glycerol

■ Oil Red O ■ Laminin ■ Hoechst

E

Fraction of oil red O (%)

**
*
*

Wild-type   GDF10 KO

□ Saline □ Glycerol

Figure 7. GDF10 Suppresses *In Vivo* Adipogenesis

(A) Microscopy images of the skeletal muscle of healthy (C57Bl6) and dystrophic (*Sgcb*-null) mice stained for GDF10 (red).

(B and D) Microscopy images of the skeletal muscle of healthy (C57Bl6) and dystrophic (Sgcb-null) mice 2 weeks after intra-muscular injection with either saline or glycerol. Sections were stained for fibrosis using α-smooth muscle actin (ACTA2, red; B) and adipocytes using oil red O (red; D).

(C) Fraction ACTA2$^+$ cells shown in (B) (n = 5–6).

(E) Fraction of oil red O$^+$ cells shown in (D) (n = 5–6). In (C) and (E), *p < 0.05; **p < 0.01. In all panels, nuclei are stained with Hoechst 33258 (blue). Data are represented as mean ± SEM. Scale bars, 200 μm.

expression of *Thbs4*. In dystrophic muscles, ISC 3 contains three clusters that express specific genes like *Ptx3*, involved in acute inflammation (Bottazzi et al., 2016), and *Cthrc1*, which is important in tissue remodeling (Wu et al., 2017). Moreover, pseudotemporal ordering of interstitial cell populations conceded a theoretical transitioning pattern between ISC 1, ISC 2, and ISC 3, as well as a shift from healthy to dystrophic muscle. ISC 3 could be heavily affected by the loss of tissue homeostasis and potentially dictates the disastrous changes during muscle degeneration. In summary, we disentangled the heterogeneity of skeletal muscle interstitial cells in pathophysiological conditions and found evidence that one specific population could be responsible for blocking aberrant fat deposition.

Within the adipogenesis, PPARγ has been identified as the master regulator. Therefore, inhibiting PPARγ is essential in order to block adipogenesis within the skeletal muscle, indirectly suggesting an effect of GDF10 on PPARγ. Contradictory to its role in fat accumulation, PPARγ is also important for mitochondrial biogenesis, switching to oxidative fiber types, myogenesis, and angiogenesis, all contributing to better muscle performance

(Amin et al., 2010; Phua et al., 2018). Thus, although GDF10 can reduce the replacement of myofibers with adipose tissue, it should be noted that it might also have a negative effect on the muscle function itself.

Furthermore, as PPARγ is considered a master regulator, its expression is controlled through multiple mechanisms, including hedgehog, Wnt/β-catenin, and bone morphogenesis protein (BMP)-mediated signaling pathways (Du et al., 2010; Platko et al., 2019; Yao et al., 2019). From our data, it is likely that GDF10 acts through one of these mechanisms, as the overexpression of GDF10 does not fully block adipogenesis. Within the CD142$^+$ ISCs, GDF10 most likely works together with other factors to inhibit PPARγ completely and thus the adipogenic differentiation of CD142$^-$ ISCs. Nevertheless, GDF10 absence in the *Gdf10*$^{-/-}$ mice resulted in fat depots within skeletal muscles that can be exacerbated by glycerol treatment. These *in vivo* results fully support the critical role of GDF10 in controlling aberrant fat depots in muscle tissues.

It remains to be determined how this interstitial remodeling takes place in dystrophic skeletal muscle and what the driving factors are. In recent light, a similar CD142$^+$ cell population that is essential for colonic epithelial stem cell function was found to be highly reduced in colitis, suggesting its broad implications in tissue homeostasis (Kinchen et al., 2018). We hypothesize that inflammation could be an essential factor of this remodeling, which suggests an important role for immune cells. We know that ISCs can be affected by the immune system because it was shown that macrophages, by secreting TGF-β, are able to inhibit the apoptosis of FAPs in muscular dystrophy (Lemos et al., 2015).

Taken together, our results shed light on the interstitial cell types of the murine skeletal muscle in health and chronic muscle

injuries and provide evidence that there is a cell population that inhibits adipogenesis. We hypothesize that the fact that this population is reduced in dystrophic muscle could be a potential cause for aberrant fat deposition that arises in patients with muscular dystrophy, although further research is necessary to be able to provide a causal link. Nevertheless, these findings are a potential explanation and might aid in developing future therapeutic approaches that block adipogenesis in the skeletal muscle and prolong the ambulation of muscular dystrophy patients.

STAR★METHODS

Detailed methods are provided in the online version of this paper and include the following:

- KEY RESOURCES TABLE
- RESOURCE AVAILABILITY
  - Lead Contact
  - Materials Availability
  - Data and Code Availability
- EXPERIMENTAL MODEL AND SUBJECT DETAILS
  - Mice
  - Human samples
  - Cell lines
- METHOD DETAILS
  - Isolation and digestion of hindlimbs
  - scRNA-seq
  - FACS isolation of the interstitial stromal cells
  - *Ex vivo* adipogenic and myogenic differentiation
  - *In vivo* experiments
  - Transwell titration experiment
  - siRNA-mediated knockdown of Gdf10
  - Viral vector-mediated overexpression of Gdf10
  - RNA isolation and quantitative PCR
- QUANTIFICATION AND STATISTICAL ANALYSIS
  - scRNA-seq data analysis
  - scRNA-seq data analysis of public datasets
  - Annotation and functional enrichment analyses
  - General statistics and plots

SUPPLEMENTAL INFORMATION

Supplemental Information can be found online at https://doi.org/10.1016/j.celrep.2020.107597.

AUTHOR CONTRIBUTIONS

Conceptualization, J.C., N.B., and M.S.; Methodology, N.B. and J.C.; Software, J.C., A.S., and S.V.; Investigation, J.C., N.B., N.G., L.D., M.C., H.G., M.B., M.M., Y.T., K.P., and M.E.M.; Resources, I.T., R.G., and R.C.A.; Visualization, J.C. and N.B.; Writing – Original Draft, J.C. and N.B.; Writing – Review & Editing, G.C. and T.V.; Funding Acquisition, J.C., N.B., and M.S.

DECLARATION OF INTERESTS

The authors declare no competing interests.

REFERENCES

Alexander, M.S., Rozkalne, A., Colletta, A., Spinazzola, J.M., Johnson, S., Rahimov, F., Meng, H., Lawlor, M.W., Estrella, E., Kunkel, L.M., et al. (2016). CD82 is a marker for prospective isolation of human muscle satellite cells and is linked to muscular dystrophies. Cell Stem Cell *19*, 800–807.

Amin, R.H., Mathews, S.T., Camp, H.S., Ding, L., and Leff, T. (2010). Selective activation of PPARgamma in skeletal muscle induces endogenous production of adiponectin and protects mice from diet-induced insulin resistance. Am. J. Physiol. Endocrinol. Metab. *298*, E28–E37.

Anders, S., Pyl, P.T., and Huber, W. (2015). HTSeq–a Python framework to work with high-throughput sequencing data. Bioinformatics *31*, 166–169.

Aryal, B., Rotllan, N., Araldi, E., Ramírez, C.M., He, S., Chousterman, B.G., Fenn, A.M., Wanschel, A., Madrigal-Matute, J., Warrier, N., et al. (2016). ANGPTL4 deficiency in haematopoietic cells promotes monocyte expansion and atherosclerosis progression. Nat. Commun. *7*, 12313.

Ashburner, M., Ball, C.A., Blake, J.A., Botstein, D., Butler, H., Cherry, J.M., Davis, A.P., Dolinski, K., Dwight, S.S., Eppig, J.T., et al.; The Gene Ontology Consortium (2000). Gene ontology: tool for the unification of biology. Nat. Genet. *25*, 25–29.

Bottazzi, B., Inforzato, A., Messa, M., Barbagallo, M., Magrini, E., Garlanda, C., and Mantovani, A. (2016). The pentraxins PTX3 and SAP in innate immunity, regulation of inflammation and tissue remodelling. J. Hepatol. *64*, 1416–1427.

Carbon, S., Dietze, H., Lewis, S.E., Mungall, C.J., Munoz-Torres, M.C., Basu, S., Chisholm, R.L., Dodson, R.J., Fey, P., Thomas, P.D., et al.; The Gene Ontology Consortium (2017). Expansion of the Gene Ontology knowledgebase and resources. Nucleic Acids Res. *45* (*D1*), D331–D338.

Costamagna, D., Berardi, E., Ceccarelli, G., and Sampaolesi, M. (2015). Adult stem cells and skeletal muscle regeneration. Curr. Gene Ther. *15*, 348–363.

Dellavalle, A., Sampaolesi, M., Tonlorenzi, R., Tagliafico, E., Sacchetti, B., Perani, L., Innocenzi, A., Galvez, B.G., Messina, G., Morosetti, R., et al. (2007). Pericytes of human skeletal muscle are myogenic precursors distinct from satellite cells. Nat. Cell Biol. *9*, 255–267.

Du, M., Yin, J., and Zhu, M.J. (2010). Cellular signaling pathways regulating the initial stage of adipogenesis and marbling of skeletal muscle. Meat Sci. *86*, 103–109.

Dube, D.K., McLean, M.D., Dube, S., and Poiesz, B.J. (2014). Translational control of tropomyosin expression in vertebrate hearts. Anat. Rec. (Hoboken) *297*, 1585–1595.

Durbeej, M., Cohn, R.D., Hrstka, R.F., Moore, S.A., Allamand, V., Davidson, B.L., Williamson, R.A., and Campbell, K.P. (2000). Disruption of the β-sarcoglycan gene reveals pathogenetic complexity of limb-girdle muscular dystrophy type 2E. Mol. Cell *5*, 141–151.

Feige, P., Brun, C.E., Ritso, M., and Rudnicki, M.A. (2018). Orienting muscle stem cells for regeneration in homeostasis, aging, and disease. Cell Stem Cell *23*, 653–664.

Frontera, W.R., and Ochala, J. (2015). Skeletal muscle: a brief review of structure and function. Calcif. Tissue Int. *96*, 183–195.

Giordani, L., He, G.J., Negroni, E., Sakai, H., Law, J.Y.C., Siu, M.M., Wan, R., Corneau, A., Tajbakhsh, S., Cheung, T.H., and Le Grand, F. (2019). High-

dimensional single-cell cartography reveals novel skeletal muscle-resident cell populations. Mol. Cell *74*, 609–621.e6.

GTEx Consortium (2015). Human genomics. The Genotype-Tissue Expression (GTEx) pilot analysis: multitissue gene regulation in humans. Science *348*, 648–660.

Hamrick, M.W., McGee-Lawrence, M.E., and Frechette, D.M. (2016). Fatty infiltration of skeletal muscle: mechanisms and comparisons with bone marrow adiposity. Front. Endocrinol. (Lausanne) *7*, 69.

Hinge, A., Xu, J., Javier, J., Mose, E., Kumar, S., Kapur, R., Srour, E.F., Malik, P., Aronow, B.J., and Filippi, M.-D. (2017). p190-B RhoGAP and intracellular cytokine signals balance hematopoietic stem and progenitor cell self-renewal and differentiation. Nat. Commun. *8*, 14382.

Joe, A.W.B., Yi, L., Natarajan, A., Le Grand, F., So, L., Wang, J., Rudnicki, M.A., and Rossi, F.M.V. (2010). Muscle injury activates resident fibro/adipogenic progenitors that facilitate myogenesis. Nat. Cell Biol. *12*, 153–163.

Judson, R.N., Quarta, M., Oudhoff, M.J., Soliman, H., Yi, L., Chang, C.K., Loi, G., Vander Werff, R., Cait, A., Hamer, M., et al. (2018). Inhibition of methyltransferase Setd7 allows the in vitro expansion of myogenic stem cells with improved therapeutic potential. Cell Stem Cell *22*, 177–190.e7.

Kinchen, J., Chen, H.H., Parikh, K., Antanaviciute, A., Jagielowicz, M., Fawkner-Corbett, D., Ashley, N., Cubitt, L., Mellado-Gomez, E., Attar, M., et al. (2018). Structural remodeling of the human colonic mesenchyme in inflammatory bowel disease. Cell *175*, 372–386.e17.

Kiselev, V.Y., Kirschner, K., Schaub, M.T., Andrews, T., Yiu, A., Chandra, T., Natarajan, K.N., Reik, W., Barahona, M., Green, A.R., et al. (2017). SC3: consensus clustering of single-cell RNA-seq data. Nat. Methods *14*, 483–486.

Kopinke, D., Roberson, E.C., and Reiter, J.F. (2017). Ciliary hedgehog signaling restricts injury-induced adipogenesis. Cell *170*, 340–351.e12.

Kuhlbrodt, K., Herbarth, B., Sock, E., Hermans-Borgmeyer, I., and Wegner, M. (1998). Sox10, a novel transcriptional modulator in glial cells. J. Neurosci. *18*, 237–250.

Kuleshov, M.V., Jones, M.R., Rouillard, A.D., Fernandez, N.F., Duan, Q., Wang, Z., Koplev, S., Jenkins, S.L., Jagodnik, K.M., Lachmann, A., et al. (2016). Enrichr: a comprehensive gene set enrichment analysis web server 2016 update. Nucleic Acids Res. *44* (W1), W90–W97.

Lachmann, A., Torre, D., Keenan, A.B., Jagodnik, K.M., Lee, H.J., Wang, L., Silverstein, M.C., and Ma'ayan, A. (2018). Massive mining of publicly available RNA-seq data from human and mouse. Nat. Commun. *9*, 1366.

Lemos, D.R., Babaeijandaghi, F., Low, M., Chang, C.-K., Lee, S.T., Fiore, D., Zhang, R.-H., Natarajan, A., Nedospasov, S.A., and Rossi, F.M.V. (2015). Nilotinib reduces muscle fibrosis in chronic muscle injury by promoting TNF-mediated apoptosis of fibro/adipogenic progenitors. Nat. Med. *21*, 786–794.

Licht, A.H., Nübel, T., Feldner, A., Jurisch-Yaksi, N., Marcello, M., Demicheva, E., Hu, J.H., Hartenstein, B., Augustin, H.G., Hecker, M., et al. (2010). Junb regulates arterial contraction capacity, cellular contractility, and motility via its target Myl9 in mice. J. Clin. Invest. *120*, 2307–2318.

Liu, L., Cheung, T.H., Charville, G.W., and Rando, T.A. (2015). Isolation of skeletal muscle stem cells by fluorescence-activated cell sorting. Nat. Protoc. *10*, 1612–1624.

Liu, N., Garry, G.A., Li, S., Bezprozvannaya, S., Sanchez-Ortiz, E., Chen, B., Shelton, J.M., Jaichander, P., Bassel-Duby, R., and Olson, E.N. (2017a). A Twist2-dependent progenitor cell contributes to adult skeletal muscle. Nat. Cell Biol. *19*, 202–213.

Liu, Y., Reynolds, L.M., Ding, J., Hou, L., Lohman, K., Young, T., Cui, W., Huang, Z., Grenier, C., Wan, M., et al. (2017b). Blood monocyte transcriptome and epigenome analyses reveal loci associated with human atherosclerosis. Nat. Commun. *8*, 393.

Lun, A.T.L., Bach, K., and Marioni, J.C. (2016). Pooling across cells to normalize single-cell RNA sequencing data with many zero counts. Genome Biol. *17*, 75.

Malecova, B., Gatto, S., Etxaniz, U., Passafaro, M., Cortez, A., Nicoletti, C., Giordani, L., Torcinaro, A., De Bardi, M., Bicciato, S., et al. (2018). Dynamics of cellular states of fibro-adipogenic progenitors during myogenesis and muscular dystrophy. Nat. Commun. *9*, 3670.

Mann, C.J., Perdiguero, E., Kharraz, Y., Aguilar, S., Pessina, P., Serrano, A.L., and Muñoz-Cánoves, P. (2011). Aberrant repair and fibrosis development in skeletal muscle. Skelet. Muscle *1*, 21.

Martin, M. (2011). Cutadapt removes adapter sequences from high-throughput sequencing reads. EMBnet. J. *17*, 10–12.

Mauro, A. (1961). Satellite cell of skeletal muscle fibers. J. Biophys. Biochem. Cytol. *9*, 493–495.

McCarthy, D.J., Campbell, K.R., Lun, A.T.L., and Wills, Q.F. (2017). Scater: pre-processing, quality control, normalization and visualization of single-cell RNA-seq data in R. Bioinformatics *33*, 1179–1186.

Mercuri, E., and Muntoni, F. (2013). Muscular dystrophies. Lancet *381*, 845–860.

Mitchell, K.J., Pannérec, A., Cadot, B., Parlakian, A., Besson, V., Gomes, E.R., Marazzi, G., and Sassoon, D.A. (2010). Identification and characterization of a non-satellite cell muscle resident progenitor during postnatal development. Nat. Cell Biol. *12*, 257–266.

Mozzetta, C., Consalvi, S., Saccone, V., Tierney, M., Diamantini, A., Mitchell, K.J., Marazzi, G., Borsellino, G., Battistini, L., Sassoon, D., et al. (2013). Fibroadipogenic progenitors mediate the ability of HDAC inhibitors to promote regeneration in dystrophic muscles of young, but not old Mdx mice. EMBO Mol. Med. *5*, 626–639.

Mueller, A.A., van Velthoven, C.T., Fukumoto, K.D., Cheung, T.H., and Rando, T.A. (2016). Intronic polyadenylation of PDGFRα in resident stem cells attenuates muscle fibrosis. Nature *540*, 276–279.

Nave, K.A., Lai, C., Bloom, F.E., and Milner, R.J. (1987). Splice site selection in the proteolipid protein (PLP) gene transcript and primary structure of the DM-20 protein of central nervous system myelin. Proc. Natl. Acad. Sci. USA *84*, 5665–5669.

Nervi, C., Benedetti, L., Minasi, A., Molinaro, M., and Adamo, S. (1995). Arginine-vasopressin induces differentiation of skeletal myogenic cells and up-regulation of myogenin and Myf-5. Cell Growth Differ. *6*, 81–89.

Pannérec, A., Formicola, L., Besson, V., Marazzi, G., and Sassoon, D.A. (2013). Defining skeletal muscle resident progenitors and their cell fate potentials. Development *140*, 2879–2891.

Pasut, A., Chang, N.C., Gurriaran-Rodriguez, U., Faulkes, S., Yin, H., Lacaria, M., Ming, H., and Rudnicki, M.A. (2016). Notch signaling rescues loss of satellite cells lacking Pax7 and promotes brown adipogenic differentiation. Cell Rep. *16*, 333–343.

Périé, S., Trollet, C., Mouly, V., Vanneaux, V., Mamchaoui, K., Bouazza, B., Marolleau, J.P., Laforêt, P., Chapon, F., Eymard, B., et al. (2014). Autologous myoblast transplantation for oculopharyngeal muscular dystrophy: a phase I/IIa clinical study. Mol. Ther. *22*, 219–225.

Phua, W.W.T., Wong, M.X.Y., Liao, Z., and Tan, N.S. (2018). An apparent functional consequence in skeletal muscle physiology via peroxisome proliferator-activated receptors. Int. J. Mol. Sci. *19*, 1425.

Picelli, S., Faridani, O.R., Björklund, Å.K., Winberg, G., Sagasser, S., and Sandberg, R. (2014). Full-length RNA-seq from single cells using Smartseq2. Nat. Protoc. *9*, 171–181.

Platko, K., Lebeau, P.F., Byun, J.H., Poon, S.V., Day, E.A., MacDonald, M.E., Holzapfel, N., Mejia-Benitez, A., Maclean, K.N., Krepinsky, J.C., and Austin, R.C. (2019). GDF10 blocks hepatic PPARγ activation to protect against diet-induced liver injury. Mol. Metab. *27*, 62–74.

Sacco, A., Doyonnas, R., Kraft, P., Vitorovic, S., and Blau, H.M. (2008). Self-renewal and expansion of single transplanted muscle stem cells. Nature *456*, 502–506.

Saccone, V., Consalvi, S., Giordani, L., Mozzetta, C., Barozzi, I., Sandoná, M., Ryan, T., Rojas-Muñoz, A., Madaro, L., Fasanaro, P., et al. (2014). HDAC-regulated myomiRs control BAF60 variant exchange and direct the functional phenotype of fibro-adipogenic progenitors in dystrophic muscles. Genes Dev. *28*, 841–857.

Sampaolesi, M., Torrente, Y., Innocenzi, A., Tonlorenzi, R., D'Antona, G., Pellegrino, M.A., Barresi, R., Bresolin, N., De Angelis, M.G.C., Campbell, K.P., et al. (2003). Cell therapy of alpha-sarcoglycan null dystrophic mice through intra-arterial delivery of mesoangioblasts. Science *301*, 487–492.

Sampaolesi, M., Blot, S., D'Antona, G., Granger, N., Tonlorenzi, R., Innocenzi, A., Mognol, P., Thibaud, J.-L., Galvez, B.G., Barthélémy, I., et al. (2006). Mesoangioblast stem cells ameliorate muscle function in dystrophic dogs. Nature *444*, 574–579.

Schaum, N., Karkanias, J., Neff, N.F., May, A.P., Quake, S.R., Wyss-Coray, T., Darmanis, S., Batson, J., Botvinnik, O., Chen, M.B., et al.; Tabula Muris Consortium; Overall coordination; Logistical coordination; Organ collection and processing; Library preparation and sequencing; Computational data analysis; Cell type annotation; Writing group; Supplemental text writing group; Principal investigators (2018). Single-cell transcriptomics of 20 mouse organs creates a Tabula Muris. Nature *562*, 367–372.

Schneider, C.A., Rasband, W.S., Eliceiri, K.W., et al. (2012). NIH Image to ImageJ: 25 years of image analysis. Nature Methods, 671–675. https://doi.org/10.1038/nmeth.2089.

Schwalie, P.C., Dong, H., Zachara, M., Russeil, J., Alpern, D., Akchiche, N., Caprara, C., Sun, W., Schlaudraff, K.-U., Soldati, G., et al. (2018). A stromal cell population that inhibits adipogenesis in mammalian fat depots. Nature *559*, 103–108.

Slenter, D.N., Kutmon, M., Hanspers, K., Riutta, A., Windsor, J., Nunes, N., Mélius, J., Cirillo, E., Coort, S.L., Digles, D., et al. (2018). WikiPathways: a multifaceted pathway database bridging metabolomics to other omics research. Nucleic Acids Res. *46*, D661–D667.

Trapnell, C., Cacchiarelli, D., Grimsby, J., Pokharel, P., Li, S., Morse, M., Lennon, N.J., Livak, K.J., Mikkelsen, T.S., and Rinn, J.L. (2014). The dynamics and regulators of cell fate decisions are revealed by pseudotemporal ordering of single cells. Nat. Biotechnol. *32*, 381–386.

Uezumi, A., Fukada, S., Yamamoto, N., Takeda, S., and Tsuchida, K. (2010). Mesenchymal progenitors distinct from satellite cells contribute to ectopic fat cell formation in skeletal muscle. Nat. Cell Biol. *12*, 143–152.

Uezumi, A., Ito, T., Morikawa, D., Shimizu, N., Yoneda, T., Segawa, M., Yamaguchi, M., Ogawa, R., Matev, M.M., Miyagoe-Suzuki, Y., et al. (2011). Fibrosis and adipogenesis originate from a common mesenchymal progenitor in skeletal muscle. J. Cell Sci. *124*, 3654–3664.

Upadhyay, G., Yin, Y., Yuan, H., Li, X., Derynck, R., and Glazer, R.I. (2011). Stem cell antigen-1 enhances tumorigenicity by disruption of growth differentiation factor-10 (GDF10)-dependent TGF-beta signaling. Proc. Natl. Acad. Sci. USA *108*, 7820–7825.

van der Maaten, L., and Hinton, G. (2008). Visualizing data using t-SNE. J. Mach. Learn. Res. *9*, 2579–2605.

Wada, E., Tanihata, J., Iwamura, A., Takeda, S., Hayashi, Y.K., and Matsuda, R. (2017). Treatment with the anti-IL-6 receptor antibody attenuates muscular dystrophy via promoting skeletal muscle regeneration in dystrophin-/utrophin-deficient mice. Skelet. Muscle *7*, 23.

Westergren-Thorsson, G., Antonsson, P., Malmström, A., Heinegård, D., and Oldberg, A. (1991). The synthesis of a family of structurally related proteoglycans in fibroblasts is differently regulated by TFG-β. Matrix *11*, 177–183.

Wosczyna, M.N., and Rando, T.A. (2018). A muscle stem cell support group: coordinated cellular responses in muscle regeneration. Dev. Cell *46*, 135–143.

Wu, Q., Yang, Q., and Sun, H. (2017). Role of collagen triple helix repeat containing-1 in tumor and inflammatory diseases. J. Cancer Res. Ther. *13*, 621–624.

Yamana, K., Wada, H., Takahashi, Y., Sato, H., Kasahara, Y., and Kiyoki, M. (2001). Molecular cloning and characterization of CHM1L, a novel membrane molecule similar to chondromodulin-I. Biochem. Biophys. Res. Commun. *280*, 1101–1106.

Yao, Q., Liu, J., Xiao, L., and Wang, N. (2019). Sonic hedgehog signaling instigates high-fat diet-induced insulin resistance by targeting PPARγ stability. J. Biol. Chem. *294*, 3284–3293.

Zhao, R., Lawler, A.M., and Lee, S.J. (1999). Characterization of GDF-10 expression patterns and null mice. Dev. Biol. *212*, 68–79.

STAR★METHODS

KEY RESOURCES TABLE

REAGENT or RESOURCE	SOURCE	IDENTIFIER
Antibodies		
Anti-ITGA7-PE-Vio770	Miltenyi Biotec	Cat#130-103-357; RRID AB_2652467
Anti-TER119 FITC	Thermo Scientific	Cat#11-5921-82; RRID AB_465311
Anti-CD31 FITC	Thermo Scientific	Cat#11-0311-82; RRID AB_465012
Anti-CD45 FITC	Thermo Scientific	Cat#11-0451-81; RRID AB_465049
Anti-SCA-1 SB436	Thermo Scientific	Cat#62-5981-80; RRID AB_2637286
Anti-ALPL PE	R&D systems	Cat#FAB1448; RRID AB_883814
Anti-CD34 eFluor660	Thermo Scientific	Cat#50-0341-80; RRID AB_10609352
Anti-CD55 PE	Biolegend	Cat#131803; RRID AB_1279267
Anti-CD142 PE	Sino Biological	Cat#50413-R001; Rabbit IgG Clone #001
Anti-CD140a APC	Thermo Scientific	Cat#17-1401-81; RRID AB_529482
SYTOX green	Thermo Scientific	Cat#S34860
Goat Polyclonal anti-CD140a	R&D systems	Cat#AF1062; RRID AB_2236897
Rabbit Polyclonal anti-ACTA2	Abcam	Cat#ab5694; RRID AB_2223021
Rabbit Polyclonal anti-CTHRC1	Abcam	Cat#ab85739; RRID AB_10712489
Rabbit Polyclonal anti-PTX3	Thermo Scientific	Cat#PA5-38595; RRID AB_2555193
Mouse Monoclonal anti-THBS4	Santa Cruz	Cat#sc-390734; Clone F7
Rabbit Polyclonal anti-PERILIPIN A/B	Sigma-Aldrich	Cat#P1873; RRID AB_532267
Rabbit Polyclonal anti-DESMIN	Abcam	Cat#ab8592; RRID AB_306653
Mouse Monoclonal anti-MYH1	Developmental Studies Hybridoma Bank, DSHB	RRID AB_2147781
Rabbit Polyclonal anti-SGCB	Abcam	Cat#ab222241; RRID AB_2185667
Rabbit Polyclonal anti-LAMININ	Sigma-Aldrich	Cat#L9393; RRID AB_477163
Bacterial and Virus Strains		
MLV_EF1a-Gdf10-myc	This Paper	GenBank: NM_145741
MLV_SF-eGFP	This Paper	N/A
Chemicals, Peptides, and Recombinant Proteins		
Collagenase II	Sigma-Aldrich	Cat#234155
Recombinant RNase Inhibitor	Takara	Cat#2313B
RLT lysis buffer	QIAGEN	Cat#1053393
Lipofectamine RNAi MAX	Thermo Fisher	Cat#13778150
Superscript III reverse transcriptase	Thermo Fisher	Cat#18080093
Critical Commercial Assays		
KAPA HiFi HotStart ReadyMix PCR Kit	KAPA Biosystems	Cat#07958919001
Magnetic Beads	CleanNA	Cat#CPCR
Nextera XT library preparation kit	Illumina	Cat#FC-131-1096
Nextera XT library index kit	Illumina	Cat# FC-131-2001
StemPro Adipogenesis Differentiation kit	Thermo Fisher	Cat#A1007001
RNeasy Plus Micro Kit	QIAGEN	Cat#74034
Platinum SYBR Green qPCR SuperMix-UDG	Thermo Fisher	Cat#11733038
Deposited Data		
Raw and analyzed data	This paper	GEO: GSE147883
Mouse reference genome NCBI build 38, mm10	Genome Reference Consortium	https://www.ncbi.nlm.nih.gov/projects/genome/assembly/grc/human/

(Continued on next page)

Continued

REAGENT or RESOURCE	SOURCE	IDENTIFIER
NCBI Gene Expression Omnibus database	(Giordani et al., 2019)	GEO: GSE110878
Tabula Muris Consortium	(Schaum et al., 2018)	Limb muscle
Scripts for Data Analysis	This Paper	https://github.com/campsj/scRNAseq_interstitium; https://github.com/campsj/scRNAseq_ISC_public
Experimental Models: Organisms/Strains		
Mouse: C57BL/6	The Jackson Laboratory	JAX: 00664
Mouse: Sgcb–/– (B6.129-Sgcbtm1Kcam/2J)	The Jackson Laboratory	JAX: 006833
Mouse: 129-Alpltm1(cre)Nagy	The Jackson Laboratory	JAX: 008569
Mouse: C57BL/6J Gdf10–/– mice	Prof. Se-Jin Lee Laboratory	N/A
B6.129X1-Gt(ROSA)26Sortm1(EYFP)Cos	The Jackson Laboratory	JAX: 006148
TNAP-CreERT mice	Prof. Giulio Cossu Laboratory	N/A
Oligonucleotides		
Stealth siRNA GDF10 (#97)	Thermo Fisher	MSS236597
Stealth siRNA GDF10 (#98)	Thermo Fisher	MSS236598
Software and Algorithms		
FlowJo software v10.6.2	Becton, Dickinson and Company	https://www.flowjo.com/solutions/flowjo/downloads
ImageJ/Fiji	(Schneider et al., 2012)	https://imagej.nih.gov/ij/
Cutadapt 1.5	(Martin, 2011)	https://github.com/marcelm/cutadapt
htseq-count 0.6.0	(Anders et al, 2015)	https://pypi.org/project/HTSeq/
Scater 1.8.4	(McCarthy et al., 2017)	https://bioconductor.org/packages/release/bioc/html/scater.html
Scran 1.8.4	(Lun et al, 2016)	https://bioconductor.org/packages/release/bioc/html/scran.html
t-SNE	(van der Maaten and Hinton, 2008)	https://lvdmaaten.github.io/tsne/
SC3 1.8.0	(Kiselev et al., 2017)	https://bioconductor.org/packages/release/bioc/html/SC3.html
Monocle2 2.12.0	(Trapnell et al., 2014)	http://cole-trapnell-lab.github.io/monocle-release/
Ensembl 84	N/A	http://mar2016.archive.ensembl.org/index.html

RESOURCE AVAILABILITY

Lead Contact
Further information and requests for resources and reagents should be directed to and will be fulfilled by the Lead Contact, Maurilio Sampaolesi (maurilio.sampaolesi@kuleuven.be).

Materials Availability
The viral vectors used for this study (MLV_EF1a-Gdf10-myc and MLV_SF-eGFP) were were cloned and produced by the Leuven Viral Vector Core.

Data and Code Availability
The single cell RNA-seq data generated during this study are available at NCBI Gene Expression Omnibus database GSE147883. Code available on github under https://github.com/campsj/scRNAseq_interstitium and https://github.com/campsj/scRNAseq_ISC_public.

EXPERIMENTAL MODEL AND SUBJECT DETAILS

Mice

All mouse experiments were conducted in strict accordance with European law and were approved by the Animal Ethics Committee of KU Leuven (P150/2014 and P169/2017). All mice were kept in specific pathogen-free conditions in individually ventilated cages.

The mouse strains used were C57BL/6J and C57BL/6J $Sgcb^{-/-}$ and C57BL/6J $Gdf10^{-/-}$ mice. All mice used in these experiments were male and between four and eight weeks old, unless specified otherwise. For lineage tracing studies, C57BL/6J $Alpl$-Cre were crossed with C57BL/6J R26-YFP. Afterward, cells from the hindlimbs were collected at two, five and eleven weeks of age (n = 4-8).

Human samples

Human male skeletal muscle biopsies were obtained from healthy (n = 3) and DMD (n = 3) subjects (ranging 14–35 years of age) during elective orthopedic surgery performed at the Department of Orthopedic Surgery of the Istituto Ortopedico Galeazzi IRCCS Milan Italy, after patient informed consent.

Cell lines

All cultured cells were isolated from male mice and cultured in high glucose DMEM medium supplemented with 20% fetal bovine serum (FBS), 10% Horse serum (HS) and 1% penicillin-streptomycin (pen-strep, all from GIBCO) (Growth Medium) on collagen-coated plates (Sigma-Aldrich). Cells were kept in a humified incubator under hypoxic conditions (5% O_2, 5% CO_2 and 37°C).

METHOD DETAILS

Isolation and digestion of hindlimbs

Tissue collection was carried out in accordance with the protocol published by Liu et al. (2015) with small alterations. In short, all hindlimb muscles were isolated by surgical dissection and finely minced. Minced muscles were digested with Collagenase II (Sigma-Aldrich, 700-800 U/ml in PBS) supplemented with 10% HS, 25 mM $CaCl_2$ and 100 U/ml pen-strep (all from GIBCO), for 90 min at 37°C in a warm water bath with agitation (60-70 rpm). At 60 and 90 min, the tissue was homogenized with an 18 and 20-gauge needle, respectively. Next, a red blood cell lysis was performed by incubating the cell pellet in the red blood cell lysis buffer (154 mM NH_4Cl, 10 mM $KHCO_3$, 0.1 mM EDTA) for 5 min, followed by a PBS wash, filtration through a 40 μm cell strainer (Corning) and centrifugation for 5 min at 400 g at 4°C.

scRNA-seq

Library preparation

LIN⁻ muscle cells were sorted single-cell by FACS in 96 well plates (4titude). Each well contained 4 μl lysis buffer (0.4% Triton X-100 in RNase-free water supplemented with 10 mM biotinylated Oligo-dT (IDT), 10 mM dNTPs (Thermo Scientific) and 0.5 U/μl RNase inhibitor (Takara)). cDNA libraries were generated based on the SMART-seq2 protocol (Picelli et al., 2014). Briefly, before mRNA was reverse transcribed, lysed cells were incubated at 72°C for 3 min and cDNA was amplified via PCR for 22 cycles. Amplification was done with KAPA HIFI Hot Start ReadyMix and purification by magnetic beads. Quantity and quality of cDNA were assessed with a Qubit fluorometer (Thermo Scientific) and Agilent 2100 BioAnalyzer with a high-sensitivity chip, respectively. Library preparation was done with the Nextera XT library prep and index kit. 100 pg of cDNA was tagmented by transposase Tn5 and amplified with dual-index primers (i7 and i5, 14 cycles). Reagents were mixed together by the Echo 555 (Labcyte) and pooled Nextera XT libraries were purified. 384 single-cell libraries were pooled together and sequenced single-end 50 bp on a single lane of a Hiseq2500 or Hi-Seq4000 (Illumina). All results related to scRNA-seq are based on freshly isolated muscle cells from C57Bl6 (healthy cells, n = 115) and $Sgcb$ null (dystrophic cells, n = 141) mice, experiments were performed on the same day.

FACS isolation of the interstitial stromal cells

The single-cell suspension was diluted to 1×10^6 cells/ml with FACS buffer (2% FBS, 10 mM HEPES and 10 mM NaN_3 at a pH of 7.2). Cells were incubated with the primary antibodies 30 min at 4°C protected from light. The following antibodies were used: TER-119-FITC (0.5 μg/10^6 cells), CD31-FITC (0.25 μg/10^6 cells) and CD45-FITC (0.25 μg/10^6 cells) for selecting the LIN⁻ population; SCA-1-SB436 (0.5 μg/10^6 cells) and/or CD140a-APC (1 μl/10^6 cells) to enrich for ISCs, ALPL-PE (0.25 μg/10^6 cells) to enrich the LIN⁻ population for MABs, Itga7-PE-Vio770 (0.15ng/10^6 cells) and CD34-eFluor660 (2.5 μg/10^6 cells) to enrich for MuSCs; CD55-PE (0.5 μg/10^6 cells) and CD142-PE (2 μl/10^6 cells) to separate the ISC populations. The cells were washed twice and stained with SYTOX green dead cell stain (1μl/ ml) to assess viability. The analysis was performed on a BD FACSCanto II HTS (BD Biosciences). Sorting was performed on the BD FACSAria III (BD Biosciences), using a 100 μm nozzle at 18 PSI or on the BD FACSMelody (BD Biosciences), using a 100 μm nozzle at 22 PSI (n = 3-4). Compensation measurements were performed for single cell stains with UltraComp eBeads compensation beads (Invitrogen #01-2222-41). Data were collected with the FacsDIVA software and analysis was performed using FlowJo software.

Ex vivo adipogenic and myogenic differentiation
Murine interstitial stromal cells

The same number of cells was sorted and seeded into flat-bottom 24 well cell culture plates (Corning #3738) coated with Collagen (Sigma-Aldrich). For adipogenic differentiation cells, we used the StemPro Adipogenesis Differentiation kit with medium changes every 3 to 4 days. Differentiation was carried out for 10 to 12 days after induction at which point the cells were stained for imaging or collected for RNA isolation. For myogenic differentiation cells MAB, FAP and MuSCs (transduced with GFP transgenic MLV viral vectors (3.325×10^6 TU/ml)) were mixed with control MuSCs at a 1:2 ratio in growth medium. The culture was carried out for 3 to 4 days after induction.

For the human ISCs, 5×10^3 CD142$^+$ and CD142$^-$ ISCs were sorted from healthy (n = 3) and DMD (n = 3) muscles and co-cultured at the bottom chamber of the transwell. For myogenic differentiation, after seeding cells on a laminin-coated surface, serum-starvation was performed for five days.

Quantification of ex vivo differentiation

Differentiated cells were fixed with 4% paraformaldehyde before staining with Hoechst33342 (Sigma-Aldrich #14533), Oil Red O (Sigma-Aldrich) and Perilipin-1 A/B (1:100) with secondary antibody anti-rabbit AF488 (Sigma-Aldrich #SAB4600234) (n = 3). Image analysis was performed in ImageJ/Fiji, lipid droplets (red) and nuclei (blue) images were filtered using a Gaussian blur (sigma equal to 2) before automatic thresholding. For myogenic differentiation, cells were stained with Hoechst33342, Desmin (1:100), and MF20 (1:20). Fluorescence images were acquired via Eclipse Ti inverted microscope (Nikon).

In vivo experiments
Myogenic differentiation potential of ISCs

5×10^6 CD55$^+$ (n = 5) and CD55$^-$ (n = 5) ISCs in 8 μl of HBSS (GIBCO) were transplanted in the *Tibialis anterior* of *Sgcb*$^{-/-}$ mice. The grafted muscles were harvested five weeks after transplantation and were snap frozen in liquid nitrogen. Serial transverse 12 μm cryostat sections were obtained from cell injected muscles and stained for human SGCB (1:50) and LAMININ (1:100).

Effect of GDF10 upon injury

C57BL/6 and C57BL/6 *Gdf10*$^{-/-}$ mice (n = 5) were injected with 50 μl of 50% glycerol in the right *Tibialis anterior*, the contralateral muscle was injected with an equivalent amount of PBS. The muscle was harvested two weeks after injury and snap frozen in liquid nitrogen. Serial transverse 8 μm cryostat sections were obtained made and stained for ACTA2 (1:200) or Oil red O and LAMININ (1:100).

Transwell titration experiment

CD142$^-$ ISCs were seeded at the bottom of a 24w transwell plate at 10,000 cells/cm^2 and CD142$^+$ ISCs in the top insert at different ratios (ranging from 5,000 to 30,000 for the titration experiment and 20,000 for other transwell experiments). Cells were differentiated as described above (n = 4).

siRNA-mediated knockdown of Gdf10

For *Gdf10* silencing, a pool of two siRNA probes (#98, #99; Thermo Scientific #1320003) was reverse-transfected to CD142$^+$ ISCs (Figure S7). 10,000 cells/cm^2 were plated with 100 nM of siRNA dissolved in 1.5% Lipofectamine RNAi MAX (Invitrogen) in Opti-MEM I reduced serum medium (Invitrogen). After 8 hours, the medium was changed normal growth medium and after 12 hours the cells were collected for determining knockdown efficiency, seeded in collagen-coated 24well plates at a density of 10,000 cells/cm^2 or seeded in collagen-coated 24well transwell inserts together with CD142$^-$ ISCs at the bottom. After 48 hours, all cell populations were treated with adipogenic differentiation medium (n = 4).

Viral vector-mediated overexpression of Gdf10

For *Gdf10* overexpression, CD142$^-$ ISCs were plated 10,000 cells/cm^2 in growth medium together with MLV-based vectors expressing Gdf10 (MLV_EF1a-Gdf10-myc) or a control vector (MLV_SF-eGFP). After 48 hours, cells were collected for determining overexpression efficiency or subjected to adipogenic differentiation and imaged at day 10 after induction (n = 6).

RNA isolation and quantitative PCR

RNA isolation of sorted and differentiated cells. Live cells were collected in RLT lysis buffer (QIAGEN) and snap frozen on dry ice. Cell lysates were homogenized with 21G syringes before RNA isolation using the RNeasy Plus Micro Kit (QIAGEN). Reverse transcription was performed using the Superscript III reverse transcriptase (Invitrogen), following the manufacturer's recommendations. Expression levels of mRNA were assessed by real-time PCR using the Platinum SYBR Green qPCR SuperMix-UDG (Invitrogen) on the fast run mode of the Viia7 Real-Time PCR system (Thermo Scientific). mRNA expression was normalized to *Rpl13a* (for all mouse experiments, if not otherwise specified) (n = 6).

QUANTIFICATION AND STATISTICAL ANALYSIS

scRNA-seq data analysis

Fastq files contained 50-bp-long single-end sequenced tags (reads) from 384 cells each were trimmed with cutadapt 1.5 (Martin, 2011). The number of tags per gene was calculated using htseq-count 0.6.0 (Anders et al., 2015). Quality control on aligned and counted reads was done with Scater 1.8.4 (McCarthy et al., 2017), cells with < 150,000 reads; < 1,500 detected genes; > 6% mitochondrial DNA and > 10% of spike-in ERCCs (Figure S1B). Cell cycle selection and read normalization were done with Scran 1.8.4 (Lun et al., 2016), cells were selected for G1 cell cycle phase and reads were normalized separately from ERCCs with parameters 'min.size = 30' (Figure S1C). For each gene, expression estimates per gene were expressed as log-transformed counts by taking the $\log^2$(counts + 1). We used the top 500 highest variable genes to obtain a 2D representation of the cells while maintaining the similarity relationships between them using t-SNE (van der Maaten and Hinton, 2008) with a perplexity of 6. Clustering was performed with SC3 1.8.0 (Kiselev et al., 2017) using k = 7 (Figures S1E–S1G). Differential expression between clusters was calculated using the nonparametric Kruskal–Wallis test, $p < 0.01$ corrected for multiple testing with a Benjamini-Hochberg False Discovery Rate (FDR) correction (Tables S1 and S4). Marker genes were selected by a binary classifier for each gene that was constructed based on the mean cluster-expression values. The area under the receiver operating characteristic (AUROC) curve was used to quantify the accuracy of the prediction. A P-value was assigned to each gene using the Wilcoxon signed-rank test, comparing gene ranks in the cluster with the highest mean expression with all others. Genes with AUROC > 0.85 and with $p < 0.01$, were defined as marker genes. Heatmaps were generated using pheatmap_1.0.10 with marker genes filtered for AUROC > 0.8 and adjusted P-value < 0.01 (Wilcoxon signed-rank test, holm correction).

For further analysis of ISCs, we additionally removed cells with > 6% of spike-in ERCCs (Figure S6C). Clustering on ISCs was performed with SC3 1.8.0 (Kiselev et al., 2017) using k = 5. Consensus, silhouette analysis and well-known marker genes supported a five-partitioning clustering (Figures S6D–S6F). We used PCA on the top 500 most variable genes to visualize the distinction between the clusters. Differentially expressed and marker genes between clusters were calculated with SC3 as mentioned above. Regressing out the genotype was done with Seurat 3.1. SCEset object was converted to a Seurat object and the scaledata function was used to regress out cell genotype (Figure S5A). The pseudotime and BEAM analysis were done with Monocle2 2.12.0 (Trapnell et al., 2014) with selected genes based on DE (standard Wilcoxon test with Holm correction) of SC3 clusters. For the pseudotime analysis a minimum spanning tree was constructed of healthy and dystrophic ISCs based on the expression pattern of 1000 genes with the first two dimensions of PCA on k-means clusters (k = 5). BEAM analysis fitted a negative binomial generalized linear model (GLM) from the ISC 2 branch to ISC 1 and ISC 3 (Figures S6K and S6L). The RNA velocity analysis was performed using velocyto. We filtered genes with a minimum average expression count lower than 0.05, fit gammas on the top/bottom 10% quantiles based and used the 20 k-nearest-neighbors in slope calculation smoothing (Figure 3F).

scRNA-seq data analysis of public datasets

scRNA-seq data of healthy murine skeletal muscle from Giordani et al. (2019) (n = 12,441) was downloaded from the NCBI Gene Expression Omnibus database (GEO, GSE110878'). The data was reanalysed with Seurat 3.1. Cells with more than 10% mitochondrial DNA were removed. Further, counts were log-normalized, the 2000 most variable features selected, data was scaled and 20 PCA dimensions were taken to perform clustering at a resolution of 0.5 and UMAP dimensionality reduction. Differential expression analysis was done by a Wilcoxon test, selected genes were at least expressed in 25% of the cells in each cluster and had a logFC treshold of 0.25. Cell type annotation was done by the following marker genes: *CD3g* (T); *CD79a* (B); *CD14* (Monocyte); *CD14, IL1b* (Macrophage); *Retnlg* (DC), *Pecam1* (endothelial), *Ly6a, Pdgfra* (FAP), *Myod1* (satellite), *Myl9* (SMMC), *Thbs4* (Tenocyte), *Plp1* (Glial) (Figure S2C). scRNA-seq data from the Tabula Muris Consortium (Schaum et al., 2018) was downloaded through the ExperimentHub package and filtered for limb muscle data (n = 4,543), cell annotation was provided by the authors. Analyzing the percentage of matching markers was done by calculating the amount of DE genes that were found per cluster in our dataset compared to the Giordani or Schaum dataset, divided by the total amount of marker genes per cluster defined in our data (Figures S2E and S2F). Integration of all datasets was done by canonical correlation analysis (CCA) with Seurat 3.1. All datasets were merged into one Seurat object, data was normalized, the 2000 most variable features were selected, and integration anchors were defined for 30 dimensions (Figures S2G–S2I). For integration of all ISC clusters, we selected the 'FAP' cluster of the Giordani data (n = 1,517) and the 'mesenchymal stem cell' cluster of the Schaum data (n = 1,127). Integrating all datasets was done in the same way as for the limb muscle data with the only difference that we used 10 dimensions to integrate anchors (Figures S5B–S5G).

Annotation and functional enrichment analyses

Enrichment analysis was performed for DE genes for LIN⁻ and ISC clusters (Table S1) using the web server Enrichr with default parameters (Kuleshov et al., 2016) and annotations provided by GO cellular biology (Ashburner et al., 2000; Carbon et al., 2017), Wikipathways (Slenter et al., 2018), or gene expression data provided by the GTEx project (GTEx Consortium, 2015) and ARCHS4 tissues (Lachmann et al., 2018) (Tables S2, S3, and S5). The combined score value is computed by multiplication of the log *p-value* from the Fisher's exact test by the z-score of the deviation from the expected rank.

General statistics and plots

All t tests and Wilcoxon rank-sum tests were unpaired and two-sided, if not otherwise specified. All boxplots were generated and displayed in R, using the geom_boxplot() function of ggplot2 with default parameters. The median value is indicated with a black line, and a colored box (hinges) is drawn between the 1st and 3rd quartiles (interquartile range, IQR). The whiskers correspond to approximately 1.5x interquartile range (± 1.58 interquartile range divided by the square root of n) and outliers are drawn as individual points. All violin plots are generated and displayed in R, using the geom_violin() function of ggplot2. Individual points or median value is portrayed by a point. All bar plots display mean values as centers and the standard deviation as error bars. All included microscopy images and macroscopic images are representative.